

---

Electronic Thesis and Dissertation Repository

---

8-28-2019 2:00 PM

## The effect of spatial averaging on dB/dt exposure values for implanted medical devices

Christopher AP Brown  
*The University of Western Ontario*

Supervisor  
Chronik, Blaine A.  
*The University of Western Ontario*

Graduate Program in Physics

A thesis submitted in partial fulfillment of the requirements for the degree in Master of Science

© Christopher AP Brown 2019

Follow this and additional works at: <https://ir.lib.uwo.ca/etd>



Part of the [Physics Commons](#)

---

### Recommended Citation

Brown, Christopher AP, "The effect of spatial averaging on dB/dt exposure values for implanted medical devices" (2019). *Electronic Thesis and Dissertation Repository*. 6512.

<https://ir.lib.uwo.ca/etd/6512>

This Dissertation/Thesis is brought to you for free and open access by Scholarship@Western. It has been accepted for inclusion in Electronic Thesis and Dissertation Repository by an authorized administrator of Scholarship@Western. For more information, please contact [wlsadmin@uwo.ca](mailto:wlsadmin@uwo.ca).

## Abstract

Magnetic resonance imaging (MRI) is a medical imaging modality that has seen continuous growth in the decades since its introduction. In conjunction with this increase in the use of MRI, there has also been a growth in the number of patients having implanted medical devices, such as pacemakers. These devices can have undesirable interactions with the MR system. The safety of these interactions must be guaranteed while ensuring that safety limits are not so conservative that they would preclude too many patients from benefiting from MRI. One factor that could make limits less restrictive is spatial averaging of the fields in MRI.

The objective of this investigation was to determine the effect that spatial averaging would have on the predicted time-varying magnetic field ( $dB/dt$ ) values within realistic MRI gradient systems. ISO/TS 10974:2018(E) contains simulated data describing the peak  $dB/dt$  values that active implantable medical devices (AIMDs) could be exposed to when within varying volumes within the bore of the MRI scanner to account for the device location dependence of the  $dB/dt$ . For devices with realistic spatial extent (e.g. a 5 cm diameter component), the  $dB/dt$  relevant for testing would need to include information about the spatial average of the  $dB/dt$  over the device.

This investigation involved the development and validation of a numerical software system to simulate the fields produced by arbitrary gradient coil designs at any point within the gradient and for any device geometry placed within that environment. The software was shown to accurately predict physical

measurements, and it was shown that the mean and peak  $dB/dt$  values differ between 2 and 17%. The difference between the peak and mean values increases monotonically with the distance from the central axis of the gradient coils.

## **Keywords**

Magnetic Resonance Imaging, Device Safety, Gradient coils, AIMDs, Simulations

## Summary for lay audience

Magnetic resonance imaging (MRI) is a medical imaging modality that is becoming more and more common. For healthy patients, it is known to be a very safe imaging modality, as it does not make use of any of the damaging radiation present in other imaging techniques like x-rays. However, when patients have an implanted medical device, like a pacemaker, as part of their treatment, this can lead to undesirable interactions with the MRI scanner. Patients with health complications benefiting from these medical devices are often those who would most benefit from MRI, so there is a need to guarantee that patient safety is assured while still allowing as many people as possible to be scanned.

One of the most important parts of every MRI system is the gradient coil. This coil produces a time varying magnetic field, called a  $dB/dt$ . In order to take full advantage of the power of MRI, it is desirable for this  $dB/dt$  value to be as large as safely possible. However, the larger the  $dB/dt$ , the greater the interaction with a medical device.

Current safety standards only refer to the peak  $dB/dt$  values that devices could be exposed to within the bore of the MRI scanner. But for devices realistic devices, the  $dB/dt$  relevant for testing would need to include the spatial average of the  $dB/dt$  over the device.

This investigation examined the effect that this spatial averaging would have on  $dB/dt$  exposure to ensure that safety limits are not too conservative, so that the most people possible can safely benefit from the diagnostic capabilities of MRI.

## Co-Authorship Statement

The work presented in chapter 2 relies on data previously collected by Christine Taracki using a probe designed by Ryan Chaddock controlled using a robotic measurement system designed by Jack Hendriks. The  $dB/dt$  coil was designed by Daniel Martire and built by the Chronik research group.

The work presented in chapter 3 has been submitted as an abstract to the International Society of Magnetic Resonance in Medicine (ISMRM). This work also seeks to be published. Brown lead the research and produced all scripts and simulations and performed all analysis. Drs. Handler and Harris wrote the code to design the gradient coils used in the simulations. Dr. Chronik funded and supervised all research.

## Acknowledgements

This thesis could not have been completed without the support and generosity of all those who have helped me not only over the past two years, but throughout my entire education.

First and foremost, thank you to my supervisor, Dr. Blaine Chronik, not only for the knowledge he has shared, but the invaluable opportunities provided by working as a member of his research group for the past six years.

I would also like to especially thank Dr. William Handler, whose knowledge, wisdom and expertise are more than made up for by his sense of humour.

Thank you to the other members of the research group during my time here, Dr. Geron Bindseil, Colin McCurdy, Justin Peterson, Christine Wawrzyn, Krzysztof Wawrzyn, Dr. Ali Attaran, Dr. Saghar Batebi and Dr. John Drozd, for their help and advice.

The apparatuses used in this research could never have been brought to life without the expert technical knowledge of Frank Van Sas, Brian Dalrymple, Ryan Chaddock, Jack Hendriks and Dereck Gignac.

Thank you to my fellow graduate students, past and present, Amgad Louka, Eric Lessard, Kieffer Davieau, Arjama Halder, Xiao Fan Ding, Diego Martinez, John Adams, Daniel Martire and Spencer Parent, with whom it has been a privilege to share friendship and my time at Western.

Thank you and much love to my parents and my sister Julia, who have been there for me every step of the way with love and support.

I would also like to acknowledge the help of my advisory committee, Dr. Lyudmila Goncharova and Dr. Giovanni Fanchini, as well as all the members of my examination committee, Dr. Corey Baron, Dr. Alexei Ouriadov and Dr. Olga Trichtchenko.

This work has been supported by the following sources of funding: NSERC, the Canada Foundation for Innovation and the Ontario Research Fund.

# Table of contents

Abstract .....	i
Summary for lay audience .....	iii
Co-Authorship Statement.....	iv
Acknowledgements.....	v
List of Tables .....	ix
List of Figures .....	x
List of Abbreviations and Symbols.....	xiv
Chapter 1: Introduction .....	1
1.1 Motivation .....	1
1.1.1 Why MRI? .....	1
1.1.2 Why is considering medical devices important? .....	2
1.2 MRI systems .....	6
1.2.1 The main magnet.....	7
1.2.2 The radiofrequency coils.....	10
1.2.3 The gradient coils.....	11
1.3 Medical devices in the MR environment .....	20
1.3.1 Types of devices .....	20
1.3.2 Device safety.....	21
1.3.3 Types of interactions.....	23
1.4 Classification of medical devices.....	29
1.5 Research objectives.....	30
Chapter 2: Validation of Biot-Savart $dB/dt$ modelling software .....	31
2.1 Introduction.....	31
2.2 Methods.....	32
2.2.1 Experimental setup.....	32
2.2.2 Simulation .....	34
2.3 Results.....	37
2.4 Discussion.....	40
Chapter 3: The effect of spatial averaging on $dB/dt$ exposure values.....	42
3.1 Introduction.....	42



3.2 Methodology .....	43
3.3 Results.....	50
3.4 Discussion.....	53
Appendix A: Simulating $dB/dt$ values .....	55
A.1 Simulating $dB/dt$ .....	55
A.2 Simulating spatial averages.....	58
A.3 Combining gradient fields.....	59
References.....	61
Curriculum Vitae .....	66

## List of Tables

**Table 3.2-1:** The spatially averaged  $dB/dt$  compared to the peaks at three different step sizes in  $z$  for the 60 cm inner diameter, 160 cm length, 45 cm imaging region coils, at a 25 cm compliance radius. The angular resolution was at 10 degrees. A  $z$  step of 10 cm was decided upon for the simulations of the final family of coils as a trade off to still have a reasonable runtime.

**Table 3.2-2:** The spatially averaged  $dB/dt$  compared to the peaks at three different step sizes in the angular spacing for the 60 cm inner diameter, 160 cm length, 45 cm imaging region coils, at a 25 cm compliance radius. A  $z$  step of 10 degrees was decided upon for the simulations of the final family of coils as a trade off to still have a reasonable runtime.

**Table 3.2-3:** The percent difference between the spatially averaged  $dB/dt$  and the peaks by component and magnitude of the  $dB/dt$  vector. Three different step sizes in  $z$  are shown for the 60 cm inner diameter, 160 cm length, 45 cm imaging region coils, at a 25 cm compliance radius.

**Table 3.3-1:** The maximum  $dB/dt$  by compliance radius for the family of coils at a slew rate of 200 T/m/s. Note that the  $dB/dt$  component labels shown above do not correspond to gradient axes but indicate the components of the  $dB/dt$  vector. The right-most three columns list the peak (no spatial averaging values) obtained for the individual  $dB/dt$  components. Note also that the magnitude column does not correspond to the quadrature sum of the peak  $x$ -,  $y$ -,  $z$ -components of the  $dB/dt$ , but rather is the peak of all the magnitudes in the calculation region.

## List of Figures

**Figure 1.2-1:** A cross-section of a modern, cylindrical bore superconducting MRI system. The three main components are the main magnet, shown in the outer layer, the gradient coil, shown in the second layer, and the RF coil, shown in yellow. Each of these three main components will be discussed in this section [16].

**Figure 1.2-2:** A sample  $k$ -space and its equivalent image [17]. Each pixel in the  $k$ -space represents a spatial frequency in the equivalent MR image, with the intensity of that pixel representing the relative importance of that spatial frequency. Note that this image only shows the real valued data. In practice, each point in  $k$ -space is a complex number with both magnitude and phase. Points closer to the center of  $k$ -space correspond to lower spatial frequencies, meaning broader, more general shapes, while points closer to edge represent high frequency, small scale details. The strength of the gradient influences the resolution of the images for a given imaging time, since it determines how far out in  $k$ -space the scanner can go, which gives higher and higher frequency information. Because of this, high gradient strength is desirable. This figure also shows that the image on the left and its  $k$ -space are equivalent in the information that they hold. One can be completely reconstructed from the other.

**Figure 1.3-1:** The three different broad categories of interactions that occur in MRI: patient/device interactions, patient/MR scanner interactions, and device/MR interactions. When evaluating device safety for patients in MRI, one must to ensure

to consider not alone interactions between the patient and the scanner, but also between devices, the scanner and the patient.

**Figure 2.2-1:** The probe used to collect  $dB/dt$  measurements. The probe had 3-axes corresponding to the Cartesian axes, with the three loops consisting of 10 loops of copper wire each with a 5.0 cm loop diameter, shown by the arrows. The set of loops hidden by the lip of the white mound corresponds to the z axis in this case, since it has its normal oriented along the bore of the coil.

**Figure 2.2-2:** The experimental setup. In the foreground is the robotic system used to collect the field data over the volume of the  $dB/dt$  coil, the cylindrical system in the midground. The grey regions contain the wire windings of the coil.

**Figure 2.2-3:** The wire pattern on the  $dB/dt$  coil. The coil is a large bore split solenoid. Visible are the two layers of wire windings, with the inner layer having 24 windings, and the outer layer having 23.

**Figure 2.2-4:** The simulated loop of the probe. It had a 5.0 cm diameter and a surface discretization of 0.5 mm, resulting it of 7860 points on the device.

**Figure 2.3-1:** The spatial distribution of the simulated  $dB/dt$  within the bore for the plane  $y = 0$  cm. Note that the z-direction is along the bore of the coil.

**Figure 2.3-2:** The spatial distribution of the measured  $dB/dt$  within the bore of coil for the plane  $y = 0$  cm. Note that the z-direction is along the bore of the coil.

**Figure 2.3-3:** The spatial distribution of percent differences between the measured and simulated values within the bore of coil for the plane  $y = 0$  cm. Note that the z-direction is along the bore of the coil. The asymmetry in the extent in the z-direction

the measurements is a result of the limitations of the reach of the positioning system.

**Figure 2.3-4:** The spatial distribution of percent differences between the measured and simulated values within the bore of coil for the plane  $z = -10$  cm. Note that the  $z$ -direction is along the bore of the coil.

**Figure 2.3-5:** A histogram of the percent differences between the measured values and the simulated data. The distribution of the errors is influenced by the precision limitations of the oscilloscope used to major the induced voltages, which in turn determine the measured  $dB/dt$  values.

**Figure 2.3-6:** Histograms of the  $dB/dt$  distributions for both the simulated (top) and measured (bottom) values. Note the systematic difference between the two. The simulation consistently underpredicts the measurements.

**Figure 2.3-7:** A comparison between the predicted field values along  $y$ , and the measured values along  $x$ . The ideal case of perfect equality is shown overlaid in red.

**Figure 3.2-1:** The 5.0 cm diameter spherical volume used as the ‘device’ in these simulations, with the points on the surface in red and the points in interior in blue. The blue points are discretized in a grid with a 5 mm separation between points along each axis. The red points are equal in number to the blue points but equally spaced over the spherical surface.

**Figure 3.2-2:** The calculation grid for the 20 cm compliance radius case. Note that the radius is slightly less than 20 cm at 17.5 cm so that the 5.0 cm diameter device volume with its center at any point on this grid will extend to 20 cm at most.

**Figure 3.2-3:** The 5.0 cm diameter spherical device in red at a single point of the surface of one compliance radius. The compliance radius it located within a single example gradient, the 60 cm inner diameter, 140 cm length, and 35 cm imaging region, for the  $z$  gradient, shown in black. The blue points, extending from -1 m to 1 m, represent each position at which the device is positioned and simulated for each coil combination.

**Figure 3.3-1:** Histogram of the  $dB/dt$  (magnitude) at all 777 points within one example coil:  $x$  gradient of 60 cm diameter, 160 cm length, 45 cm imaging region coil at a 25 cm compliance radius. Values are given as  $dB/dt$  per unit slew rate of the gradient axes. For a 200 T/m/s scanner system, the values above need to be multiplied by 200.

**Figure 3.3-2:** Histogram of all the data across all the coils (and all compliance volumes) with the 95th and 99th percentiles shown (0.352 T/s per slew rate and 0.443 T/s per slew rate). For a 200 T/m/s scanner system, the values above need to be multiplied by 200.

**Figure 3.3-3:** The peak spatially averaged  $dB/dt$  value across each coil in the simulation space at 4 different compliance radii. Values are given as  $dB/dt$  per unit slew rate of the gradient axes. For a 200 T/m/s scanner system, the values above need to be multiplied by 200.

## List of Abbreviations and Symbols

AIMD	Active implantable medical device
ASTM	American Society for Testing and Materials
B	Magnetic flux density
CT	Computed tomography
$dB/dt$	Time-varying in magnetic field
FDA	Food and Drug Administration
ISO	International Organization for Standardization
MRI	Magnetic resonance imaging
NMR	Nuclear magnetic resonance
PET	Positron emission tomography
PNS	Peripheral nerve stimulation
RF	Radiofrequency
TE	Echo time
TR	Repetition time
TS	Test standard

# Chapter 1: Introduction

This chapter introduces Magnetic Resonance Imaging (MRI) as an imaging modality and explains how some of the components within the scanner required to produce images can interact with medical devices. These interactions must all be considered when trying to classify the safety of devices for use in MRI, which determines whether patients who have active implantable medical devices (AIMDs), for example, can undergo an MR imaging procedure. A brief overview of the entire MRI assembly is given. The electromagnetic interactions that these devices experience with the MR system will be reviewed, focusing mainly on the interactions with the subsystem called the gradient coils. The chapter concludes with a description of the research objectives of this thesis.

## 1.1 Motivation

### 1.1.1 Why MRI?

Magnetic resonance imaging, or MRI, is a medical imaging modality. It is desirable because it provides excellent soft tissue contrast at high resolution without the use of ionizing radiation, or invasive intervention like biopsy [3]. In fact, MRI scans can even be used to identify tumors or bone fractures that are too small for other types of imaging like x-ray imaging [4].

Ionizing radiation includes any particle incident on the patient of sufficient energy to ionize molecules like DNA inside cells. This ionization can lead to



irreparable damage at higher doses. For example, computed tomography (CT), another widespread medical imaging modality, makes use of x-rays, which are high energy photons. In positron emission tomography (PET), gamma rays, which are photons of even greater energy than x-rays, are emitted, among other particles. In such imaging modalities, patient exposure to radiation must be carefully monitored to ensure safety [5].

MRI does not require any such exposure limitations. If established safety standards are followed, a patient could be scanned every day with no adverse effects on their health. These safety standards, and the associated safety concerns, have inspired the topic of investigation of this thesis, and will be discussed in more detail in later sections of this chapter.

Because of the advantages of MRI, millions of MR imaging exams are now conducted globally every year [32]. In Canada alone, around 1 million exams were performed in 2007. That number increased to 1.7 million MR exams conducted in 2012 [6], and increased further in 2017, with an estimated 1.86 million MRI examinations performed [7].

### **1.1.2 Why is considering medical devices important?**

As standards of health care improve and new forms of treatment are developed, there is not only an increase in the number of MRI scans performed, but it is increasingly common for patients to have implanted medical devices as a part their treatment. Millions of patients receive some type of implant each year, such as

cardiac implants (i.e. pacemakers and implantable cardioverter defibrillators). There were over 370,000 implants of cardiac pacemakers in the United States in 2003 [8], and over 135,000 implants of cardiac systems in Canada in 2006 [10, 11], and this only for one of the many categories of device (see section 1.3.1). The congruent growth in MRI availability and device use makes device safety within MR an important problem.

As previously mentioned, a healthy volunteer could be scanned every day with no adverse effects. However, because of their different material composition, medical devices, they will behave differently than biological tissues when within the complex electromagnetic environment of the scanner. These differences in behavior must be characterized prior to any imaging procedure. Devices can experience strong forces, heating, vibration, and operational failure. In addition to direct patient safety concerns, the presence of devices can affect image quality, reducing diagnostic effectiveness [13]. Later sections in 1.3.3 will go into these hazards in more detail.

Since the individuals who get medical implants already have compromised health, they are often those who would most benefit from the diagnostic capabilities of MRI to monitor their health and to track the effectiveness of treatment. Because of this, it is essential that MRI is safe and accessible for as many patients as possible. For patients with the aforementioned cardiac implants, 50 to 75% are expected to be referred to an MRI over the lifetime of the device in order to track the current status of their health. However, in the United States alone, it is estimated that 200,000 patients were denied an MRI due to the presence of implanted cardiac

systems in 2004 [8]. Understanding these hazards is thus of vital importance to ensure patient safety during scanning procedures, while also ensuring that safety standards are not so restrictive that patients who could still benefit from an MRI are being denied. Labeling provided by device manufacturers must be accurate so that medical professionals can make an appropriate informed decision when determining whether a patient may undergo an MR procedure.

The standards governing the safety of medical devices are decided upon by the regulatory bodies ASTM (American Society for Testing and Materials) and ISO (International Organization for Standardization) [20]. Under these organizations, committees are formed to investigate interactions that devices can experience and to quantify their impact on patient health. As new investigations are performed and interactions are better understood, these safety standards are subject to change, with revisions published every several years.

There is already such a wide array of devices (see section 1.3.1) and MRI systems that there are far too many scenarios to physically test [22], and there are new devices are also being developed constantly. Regulatory labelling often makes use of physically validated computer simulations to model devices and MRI systems. This aids in identifying a manageable number of worst-case scenarios under which devices should be physically tested.

However, when considering safety scenarios, there must necessarily be a balancing act between ensuring patient safety with respect to medical devices in MRI and allowing as many patients as possible to benefit from MRI. If only worst-case scenarios are considered and used in every situation, standards become too

restrictive. This reduction in accessibility reduces the benefit of MRI as a diagnostic tool.

This thesis seeks to develop a computer simulation for modeling the magnetic environment produced by one of the MRI subsystems, the gradient coils, across any arbitrary system design. The simulation tool is then used to evaluate the effect that spatial averaging will have on the time-varying field exposure values when compared to the peak exposure. It is predicted that the decrease in exposure between the two will ensure that safety standards are not too conservative, and that regulatory bodies have as much information as possible when deciding about labeling of devices.

## 1.2 MRI systems

The research included in this thesis does not pertain to any new developments in imaging or image processing. It is dedicated to ensuring that new advances in imaging can be performed safely. To that end, discussion of MRI is limited to a description of the magnetic environment necessary to image, and how this environment can lead to safety concerns. For a more advanced discussion of the process of image acquisition in MRI, refer to *Magnetic resonance imaging: Physical principles and sequence design*, [1] in addition to a more detailed description of the topics covered in this section.

Modern MRI systems are very complex and require many independent subcomponents in order to create an image. A typical MR scanner will contain several magnets: the main magnet, the radiofrequency (RF) coils, and the gradient coils, each of which will be outlined in this section. Each of the different fields in MRI interact with patients and implanted devices differently and have their own associated safety concerns, as will be discussed in section 1.3.

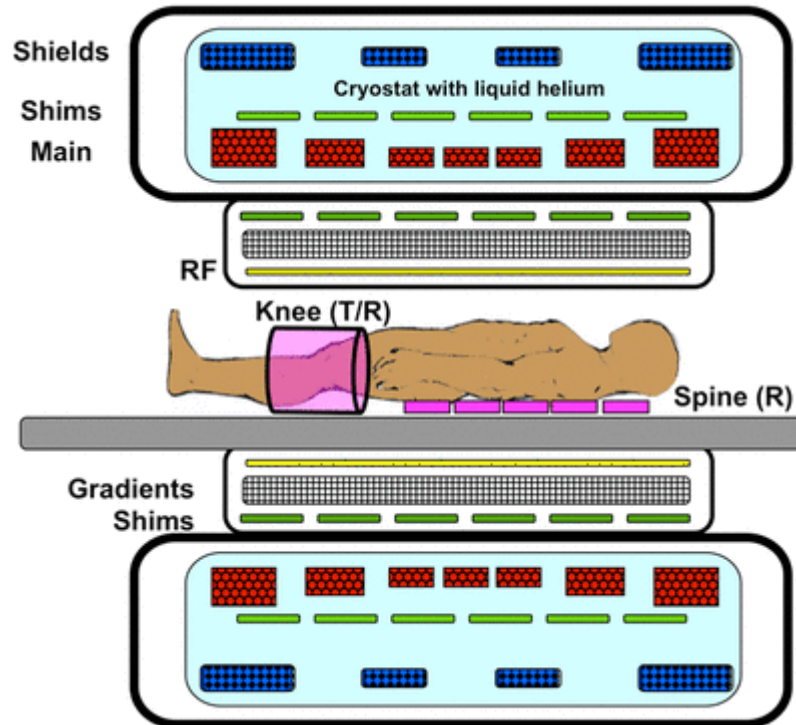


**Figure 1.2-1:** A cross-section of a modern, cylindrical bore superconducting MRI system. The three main components are the main magnet, shown in the outer layer, the gradient coil, shown in the second layer, and the RF coil, shown in yellow. Each of these three main components will be discussed in this section [16].

### 1.2.1 The main magnet

Magnetic resonance imaging operates on the principle of nuclear magnetic resonance (NMR). Imaging via NMR is possible because of the presence of unpaired nucleons in the nuclei of atoms inside the body, producing a net spin and magnetic moment in that nucleus. Most clinical MRI relies on the resonance of protons found in water molecules throughout the body. Because of the abundance of water in biological tissues, among other considerations, these have been found

to produce the best signal. Note that it is possible to obtain information similarly using any atom with a net magnetic moment, such as carbon-13 or sodium-23.

When discussing MRI, it is common to consider the behaviour of nuclei as described by classical physics. On its own, a single nucleus will not produce a very strong signal. In the classical analogy, the magnetic moments of many atoms align with the external field, producing a net magnetization within a sample. In MRI, this initial external field is produced by the main magnet. It is referred to as  $B_0$ , where  $B$  is the standard variable in electromagnetism used to represent the magnetic flux density, measured in tesla (T), and the subscript is used to emphasize its static nature within the MR scanner. Clinical MR systems vary in main magnetic field strength from 0.2 T to 10.5 T systems.

Nuclei that possess net magnetic moments will produce an electromagnetic signal when perturbed by a specifically designed magnetic field oscillating at an intrinsic resonant frequency. The rate of precession ( $\omega_0$ ) of the magnetization about the field in MRI is called the Larmor frequency, and it depends on the field strength ( $B_0$ ) and a nuclei dependent proportionality factor called the gyromagnetic ratio ( $\gamma$ ). In the presence of other fields, the  $B_0$  term is replaced by the net magnetic field that the nuclei experience.

$$\omega_0 = \gamma B_0 \quad (1.2-1)$$

For protons, which are found unpaired in every water molecule, the gyromagnetic ratio is 42.577 MHz/T. This means that in a 1 T field, they would resonate at 42.577 MHz. Because of this high frequency, the specially designed

fields needed to produce this resonance are radiofrequency (RF) fields. The coils used to produce these fields are discussed in the next section. The gyromagnetic ratio of these protons is also higher than that of other nuclei that can be used in imaging, like carbon-13 and sodium-23. This produces a stronger signal in the receiver and makes it easier to spatially distinguish information.

At higher  $B_0$  fields, in addition to the increased resonant frequency, a greater magnetization linearly proportional to the field is produced. In a paramagnetic material like water, this relationship is described by Curie's law.

$$\vec{M} = C \frac{\vec{B}}{T} \quad (1.2-2)$$

The magnetization ( $M$ ) is described in amperes per meter and is dependent on a material specific Curie constant ( $C$ ) in kelvin amperes per tesla meter, the magnetic flux density ( $B$ ) in tesla, and the temperature ( $T$ ) in kelvin. [1] This greater magnetization produces a stronger signal, increasing the signal-to-noise ratio, making it easier to acquire better quality images. However, higher  $B_0$  field strength magnet systems produce greater heating, have a greater sensitivity to field inhomogeneities, and cost much more.

In order to produce such high fields with a high magnetic field homogeneity over a large volume, the main magnets in modern MRI scanners have evolved to be cylindrical in shape, consisting of loops of superconducting wire wound around the bore. The main windings of this magnet are shown as the red bundles in the outer layer of figure 1.2-1. When a constant current is passed through the wires, a magnetic field is produced, as described by the Biot-Savart law (1.2-3).



$$\vec{B}(\vec{r}) = \frac{\mu_0}{4\pi} \int_C \frac{I \vec{dl} \times \hat{r}'}{|\vec{r}'|^2} \quad (1.2-3)$$

Here,  $\vec{B}$  is again the magnetic flux density described in tesla,  $\mu_0$  is the vacuum permeability in henries per meter,  $I$  is the current in amperes,  $\vec{dl}$  is an infinitesimal length of the wire conductor in meters, and  $\vec{r}'$  is the vector representing the distance between the conductor element and the point at which the  $\vec{B}$  field is calculated.

The main magnet is designed such that the  $B_0$  field is oriented along the axis of the bore of the magnet. When describing directions in MRI, the convention is to orient the cartesian  $z$ -axis to be in the same direction as the  $B_0$ . This field is always on, and extends beyond the bore of the scanner itself, with significant fringe field which can extend several meters into the surrounding environment [26].

### 1.2.2 The radiofrequency coils

The radiofrequency (RF) coils are responsible for both the resonant excitation of nuclei and acquisition of the MR signal. RF coils produce an oscillating magnetic field, referred to as  $B_1$ . This field must have some component of its magnetic field perpendicular to the  $B_0$  field of the main magnet. When this field is applied, it causes the magnetization of the sample to rotate away from its thermal equilibrium along  $z$ . How much it changes will depend on the amplitude and duration of the RF pulse. This results in energy being deposited in the sample as heat via induction. The RF frequency is tuned to the Larmor frequency of the nuclei being imaged, which is 42.577 MHz/T for proton imaging.

After the application of the  $B_1$  field, the magnetizations will have some component in the plane perpendicular to  $z$ , which is what is detected and constitutes the MR signal. The detector can be the same coil that transmitted the field, or a separate coil within the scanner. According to Faraday's law (1.2-4), the time-varying magnetic field will induce an electric field,  $\vec{E}$ , in a conductive loop. This produces a measurable voltage and is the principle upon which the MR signal is acquired.

$$-\frac{\partial \vec{B}}{\partial t} = \vec{\nabla} \times \vec{E} \quad (1.2-4)$$

### 1.2.3 The gradient coils

If only the main magnetic field were present, all nuclei would experience the same field, so they would precess at the same Larmor frequency. Recall from equation 1.2-1 that the resonant frequency depends on both the gyromagnetic ratio and the field strength. The resultant MR signal would not contain differentiable information about tissues within the body of the patient. Having the two systems that have been presented so far, the main magnet and the RF coils, is sufficient to excite a nuclear magnetic resonance (NMR) signal, but it is not enough for medical imaging.

In order to encode spatial information about tissues within the body, a secondary magnetic field is needed on top of the main magnetic field. This additional field is produced by magnets called gradient coils. These coils produce a field that varies linearly as a function of position over the region of interest, or imaging region. This changes the net field in the same direction as the static field,

i.e. the  $z$ -component of the field. The field varies not only spatially, but temporally. The time-varying change in the magnetic field at a point in space is called  $dB/dt$ . A higher  $dB/dt$  is produced by having either a greater gradient strength, a greater rate of change of the gradient field, or both. The need for stronger such gradient fields, and gradient coils able to vary their field more quickly, will be motivated in this section.

Since nuclei at different spatial positions experience different magnetic environments, they resonate at different frequencies, as described by equation 1.2-1. The fields produced by the gradient coil are smaller than the main field, only a few millitesla, but since the gyromagnetic ratio is so large for protons, small differences in field can produce meaningful differences in resonant frequency.

The gradient coils used to perform spatial encoding in MRI consist of three separate resistive coils which vary the  $z$ -component of the field as a function of  $x$ ,  $y$ , and  $z$ , each with their own gradient strength  $G_x$ ,  $G_y$ ,  $G_z$ , respectively. Since the field is designed to vary linearly as a function of position over the region of interest, gradient strength is described in units of tesla per meter. When these fields are combined with the field of the main magnet,  $B_0$ , the field at any point  $(x, y, z)$  in space at some time can be described by the vector:

$$\vec{B}(x, y, z) = \begin{pmatrix} 0 \\ 0 \\ B_0 + G_x x + G_y y + G_z z \end{pmatrix} \quad (1.2-5)$$

Since the rate of precession depends on this net field, it can be used to set the resonant frequency at a point in space. The gradients fields are produced in

pulses synchronized with the RF field, which is tuned to excite a specific region of interest. A specific combination of gradients and RF pulses is referred to as a pulse sequence. Since the nuclei will be oscillating at different frequencies, a phase difference will start to accrue between any two spatially distinct groups of nuclei. This phase difference is proportional to the separation between the two groups, as well as to the gradient strength and duration ( $\tau$ ), i.e. the time integral of the gradient pulse. The stronger the gradient, the greater the difference in field will be between two points. The greater the difference in field, the greater the difference in resonant frequency, so a greater phase will accumulate.

Because the magnetic field is precisely controlled, the expected precession frequency at any point in space will be known, as well as the phase accumulation at any points relative to each other dependent on their distance from the geometric center of the magnet (isocenter). This can then be cross-referenced with a mathematical operation called the Fourier decomposition of induced voltage signal in the receiver as a function of time. The Fourier transform allows a time dependent signal to be decomposed into its constituent frequencies and phases and shows how much each contributed to the total signal relative to the others. In doing this Fourier transform of the signal, the scanner can determine what spatial locations contributed more to the signal, and thus create the intensity map of proton density or signal strength which becomes the greyscale MR image.

Equation 1.2-6 expresses the phase difference in mathematical terms for an idealized gradient pulse. Note that in practice, a perfectly square gradient pulse (a gradient that is instantly turned on and off) can not be obtained due to hardware

limitations on the rate at which the field can be ramped, and the phase accumulation is more generally described by the time integral over the duration of the pulse rather than a simple multiplication of the gradient strength and duration. The quantity in brackets in equation 1.2-6 is singled out because of its importance in controlling the image acquisition process. This factor has units of spatial frequency, so the convention in physics is to refer to it by the variable  $k$ . Here, the  $k$ -value is defined for a gradient along  $x$ , but it can be extended to  $y$  and  $z$  the same way.

$$\varphi(x) = \gamma G_x x \cdot \tau = 2\pi \left( \frac{\gamma}{2\pi} G_x \tau \right) x \quad (1.2-6)$$

Returning to the precessing spins, according to Faraday's law (1.2-4), the induced voltage in the detector will be sum of all the different precessions produced by the gradients. In MRI, these signals are detected at some 'echo time' ( $TE$ ). For some MRI pulse sequences, after the initial excitation, the spins are allowed to dephase, and then they are rephased before signal acquisition, producing an 'echo' in signal. The detected signal from the RF coils is then demodulated from the carrier RF frequency, taking the form:

$$S(t) \propto \int \rho(\vec{r}) e^{i\varphi(\vec{r})} dV \int e^{i\omega t} d\omega \quad (1.2-7)$$

In this case, the integral over frequency in the second term reduces to a proportionality constant at the echo time. For the single gradient along  $x$ , the signal from the volume can be decomposed then expressed as a function of  $k_x$ , from the relationship in equation 1.2-6, with  $k$  being the term in brackets:

$$S(TE, k_x) \propto \int \rho(x) e^{i2\pi k_x x} dx \int \rho(y) dy \int \rho(z) dz \quad (1.2-8)$$

The oscillating voltage in the detector is further decomposed via Fourier analysis. The proton density distribution as a function of position along  $x$  can be obtained by an inverse transformation of the signal as a function of  $k_x$ :

$$\rho(x) = \mathcal{F}^{-1}\{S(t = TE, k_x)\} \quad (1.2-9)$$

In MRI, this process is extended to three dimensions by the other two gradient axes, so the signal is a 3D spatial frequency space, referred to as  $k$ -space. With data from the three axes collected, a 3D proton density can be retrieved from the 3D inverse Fourier transform of the  $k$ -space data. When the pulse sequence is repeated with different values for  $k_x$ ,  $k_y$ , and  $k_z$ , a full sampling of the Fourier transform of the proton density is acquired.

Recall that the values of  $k$  describe spatial frequencies. From the definition of  $k$ , as shown in 1.2-10, to encode higher spatial frequencies within some time  $\tau$ , a stronger gradient is needed. The maximum spatial frequency that can be encoded determines the resolution of the image. Thus, there is a desire to have stronger gradient fields in order to be able to capture smaller details within tissues to obtain better diagnostic information.

$$k_i = \frac{\gamma}{2\pi} G_i \tau, \quad i = x, y \text{ or } z \quad (1.2-10)$$

The  $k$  parameter also depends on the gyromagnetic ratio. If imaging using nuclei other than simple protons is to be performed, in order to acquire the same  $k$ -space information, stronger gradients would be needed, because it takes more to get the same phase difference to accrue.

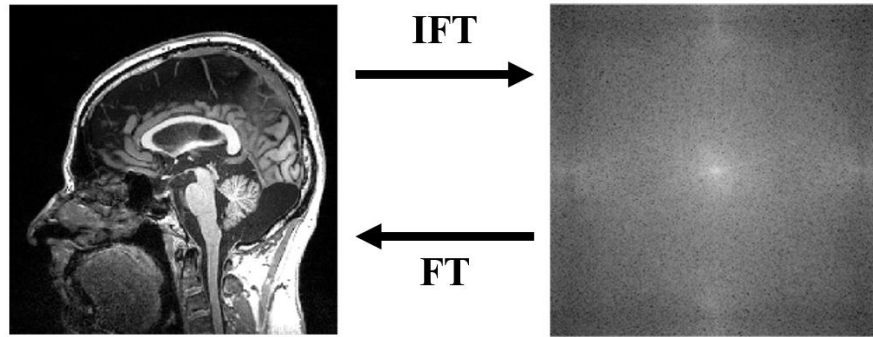


**Figure 1.2-2:** A sample  $k$ -space and its equivalent image [17]. Each pixel in the  $k$ -space represents a spatial frequency in the equivalent MR image, with the intensity of that pixel representing the relative importance of that spatial frequency. Note that this image only shows the real valued data. In practice, each point in  $k$ -space is a complex number with both magnitude and phase. Points closer to the center of  $k$ -space correspond to lower spatial frequencies, meaning broader, more general shapes, while points closer to edge represent high frequency, small scale details. The strength of the gradient influences the resolution of the images for a given imaging time, since it determines how far out in  $k$ -space the scanner can go, which gives higher and higher frequency information. Because of this, high gradient strength is desirable. This figure also shows that the image on the left and its  $k$ -space are equivalent in the information that they hold. One can be completely reconstructed from the other.

Recall that the  $dB/dt$  value is increased by having a stronger gradient field, having a faster switching gradient, or both. In many situations, the  $dB/dt$  is has a strict, more readily quantifiable upper limit. Consider that since the gradient coils are resistive magnets, as current is passed through them during a pulse sequence, power will be deposited. To produce a stronger gradient field, more current needs to be applied, producing greater power deposition and thus heating within the coil itself. For a longer pulse sequence, more power would be deposited. Certain

application could be limited by the cooling available to the resistive gradients, since the coil must not be allowed to heat up so much that it is damaged. The  $dB/dt$  can also be limited by peripheral nerve stimulation (PNS), which will be discussed briefly in section 1.3.3.3.

For pulses in certain parts of sequences that aren't repeated as quickly, like a diffusion weighted sequence, a stronger gradient strength can be used without pushing the  $dB/dt$  to an extent that PNS is a concern. In this type of sequence, having stronger gradients is desirable because it allows the encoded data to be more sensitive to the diffusion of molecules, helping identify lesions within the body or nerve tracts within the brain [1].

Returning to the definition of the definition of  $k$  in equation 1.2-10, to produce a fully sampled image, every point in  $k$ -space should be acquired. The most basic way that this data is collected is using a Cartesian sampling method, though more advanced methods exist. In Cartesian sampling, the data is collected one row at a time, where each row is collected around the echo time (TE), and the time between each row is some repetition time (TR).

The time it takes to acquire an image is in part determined by how fast the gradient coils can switch, since faster coils are able to produce shorter TEs. With scans often taking in excess of half an hour, it is desirable to have even faster gradients, especially for fast imaging techniques like echo planar imaging (EPI). In these cases, even a relatively weaker gradient strength can produce a high  $dB/dt$  because of the rate of switching of the field.



The strength and speed of a gradient coil are described by its slew rate. The slew rate is determined by the maximum gradient amplitude divided by the time it takes to reach that peak gradient strength, in units of T/m/s. Unlike the superconducting coils used in the main magnet, since gradient coils are resistive magnets and produce a lot of heat during operation, and pulses are kept relatively short for many types of imaging.

Even the fastest gradient coils available operate at relatively low frequencies compared to the RF fields. Gradients are within the range of human hearing, in the lower kilohertz. Because of this low frequency, the system is well approximated as quasi-static. Thus, no wavelength effects or retarded potentials need to be considered when calculating the gradient fields, unlike at RF frequencies, where the wavelengths are on the scale of objects within the scanner, and the quasi-static approximation is not applicable. The time variation for gradients is completely separable from the spatial variation. The frequency of oscillations is related to the wavelength through:

$$\lambda = \frac{c}{f} \quad (1.2-11)$$

Here,  $\lambda$  is the wavelength in meters and  $c$  is the speed of light. For a 5 kHz frequency, for example, the wavelength would be orders of magnitude greater than the scale of the body within the scanner. Therefore, the presence of biological tissue has no effect on the predicted  $dB/dt$  values at any point within the scanner, and fields can be calculated as though the bore of the scanner were simply at vacuum. For more information on how these fields are calculated, refer to the appendix.

The  $dB/dt$  produced by the coil described in this section has an impact on device safety. The greater the  $dB/dt$ , the greater the effect. However, ensuring device safety is not simply a matter of keeping  $dB/dt$  as low as possible. As has been shown, there is a competing desire for stronger and faster gradients for imaging, and thus there is a need to ensure that  $dB/dt$  limits are not too conservative for new imaging techniques to be developed and used.

## 1.3 Medical devices in the MR environment

This section will provide some background on the breadth of the medical devices relevant for consideration in MR safety, the interactions devices could experience with the MR system, the types of classification given to these devices, and current safety standards.

### 1.3.1 Types of devices

In the context of MR safety, a medical device is anything within the MRI environment that is neither part of the MR system or a biological part of the patient. The MRI environment is typically defined as the room in which a scanner is located [3]. More than 1,700 types of devices, 500,000 medical device models, and 23,000 manufactures are regulated by the ASTM [22]. This wide array devices includes:

- Permanent medical implants (e.g. orthopedic implants like metallic joint replacements, pacemakers, deep brain stimulators)

There are also devices that are removable, but are nonetheless useful when employed in conjunction with an MR scan:

- Physiological monitors used to run medical diagnostic tests in conjunction with the MRI scan (EEG, blood-pressure monitoring)
- Non-MR-based imaging or therapy modalities (PET, radiotherapy)
- MR-guided interventional systems (surgical robotics)

- Stimulus presentation and monitoring systems used in scientific studies (visual goggles and mirror systems) [24].

Medical devices can be additionally classified as passive devices, which perform their function without electrical power (e.g. orthopedic implants), and active devices, which involve electrical power. (e.g. a cardiac pacemaker). These are referred to by the acronym AIMD, meaning active implantable medical devices, and are of particular interest for the purposes of this investigation [25].

Note that since the MRI environment extends beyond the bore of the scanner itself, every object in the scanner room must be carefully considered. The main magnetic field is always on, and significant fringe field can extend several meters into the surrounding environment [26]. Care must be taken to avoid bringing metallic objects such as oxygen tanks into the room, as they may become projectiles, causing serious bodily harm or death to anyone in their path [27].

### **1.3.2 Device safety**

When evaluating safety in MRI, every possible physical interaction must be considered, as failure to do so can mean the difference between life or death. There are not only interactions between the patient and the scanner, but interactions with any medical devices present. Many devices when within the MR environment can present a danger to the subject, and/or interfere with the normal operation of the MR scanner [28, 29]

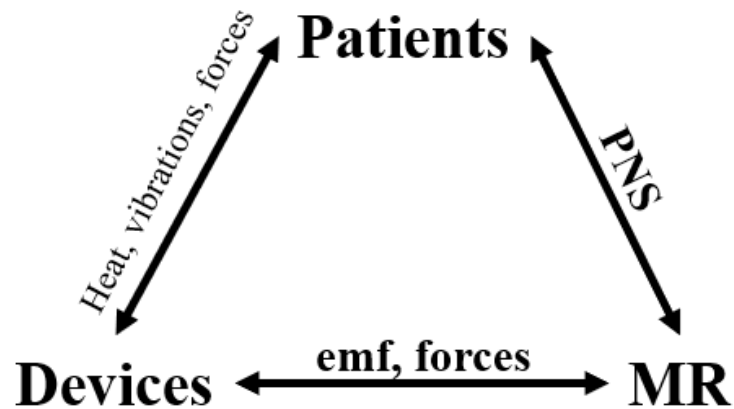


**Figure 1.3-1:** The three different broad categories of interactions that occur in MRI: patient/device interactions, patient/MR scanner interactions, and device/MR interactions. When evaluating device safety for patients in MRI, one must to ensure to consider not alone interactions between the patient and the scanner, but also between devices, the scanner and the patient.

MRI has a strong record of patient safety. Most incidents that occur are the result of a failure to follow already established operational safety guidelines rather, than accidents resulting from unprecedented interactions. More than 100,000,000 diagnostic procedures have been completed since its introduction [30], with nearly 35,000,000 performed annually in the United States alone [31], with approximately seven deaths resulting as a direct consequence of some aspect of the MR procedure [32-34].

Because of their material composition, medical devices will behave differently than biological tissue in the magnetic environment of the MRI scanner. Devices can interact in ways that can pose a significant safety risk, so they must be tested extensively before hand. These interactions will be described in the following section.

### 1.3.3 Types of interactions

The interactions between a device and the MR system are complex, and extensive testing and analysis is required to determine the conditions under which the device can be safely used within the MR environment. When a medical device is within this MR system environment it can experience forces and torques, heating, and it can cause distortions in the images due to field inhomogeneities around the device [13].

No two MR systems are identical, so there is a wide variety of magnetic environments that must be considered. Even for mass produced scanners, installation on site can require a setup configuration unique to that location, depending on how closely manufacturing tolerances are controlled. Possible interactions depend on field strength, field uniformity, pulse sequences parameters, unique patient physiology, and specific medical devices.

Many factors affect a device's behaviour. Its material composition determines parameters such as its electrical and thermal conductivity, which influences its electromagnetic interactions. Certain device geometries increase heating and torques. Position and orientation within the MR environment are also important, since exposure to the static, RF and gradient fields are spatially dependent. Devices can experience forces, torques, heating, vibration, and operational failure [25]. The standards for each type of interactions are described in [25, 38, 39, 40].

### **1.3.3.1 Main field interactions**

The effect of cumulative exposure to the strong, static, magnetic fields present in MRI has been studied extensively and has been shown to have no hazardous effects on human health when in the absence of foreign materials [32].

However, medical devices within the static main field of the scanner can experience magnetic forces and torques, depending on their material composition. Torque will tend to align the long axis of a medical device with the direction of the static magnetic field. Magnetic forces will pull magnetic materials present in the MR environment, such as oxygen tanks, toward the scanner, since a gradient in the static field strength around the scanner as the field falls off with distance induces displacement forces [12, 38, 42]. If a device implanted inside a patient experiences such forces, it could lead to fatal internal damage [32-34]. If the object is ferromagnetic, it can experience an induced force strong enough to become a projectile [27]. Stronger magnetic fields produce stronger forces and torques [41].

Any patient to be imaged must undergo an extensive medical survey to ensure that no unknown foreign materials are present within their body. For example, a lifelong metal worker may have accidentally accumulated small metallic shards in sinuses from grinding work [43].

When MR safety is considered, materials used in the manufacture of medical implants are chosen so that it will interact as little as possible with this field.

### **1.3.3.2 RF field interactions**

For RF frequency electromagnetic fields, the wavelengths are on the scale of objects within the scanner, leading to potentially significant interactions with body tissues and medical devices. RF fields deposit power in the human body even when no device is present, so imaging parameters are constrained to limit this. In medical devices, it can produce localized heating due to resistive losses of current flow even through the small electrical conductivity of tissues [12].

Power deposition is quantified by the specific absorption rate (SAR), measured in watts per kilogram of mass [25]. When a conducting medical device is present, the interactions are even stronger, and the RF field leads to greater heating [40]. SAR is related to the square of the main magnetic field, square of the flip angle, square of the patient radius, patient conductivity, and the RF duty cycle [36].

Medical devices can also cause increased electric fields around the device, leading to higher levels of SAR, heating biological tissue near the device [15]. RF heating is most prominent in long, extended devices which are of a resonant length for the frequency used.

### **1.3.3.3 Gradient field interactions**

As described in section 1.2.2, gradient coils produce a time-varying magnetic field, or  $dB/dt$ , which will induce an electric field according to Faraday's law. The



stronger the  $dB/dt$ , the greater the effect. This can have several consequences in the context of MRI.

Even when no device is present,  $dB/dt$  can affect body tissues. Since tissues are small compared to the gradient wavelengths, there is little absorption [5]. However, when the electric fields induced by the  $dB/dt$  are strong enough near nerves within the body, they can produce an action potential which involuntarily activates the nerve. This phenomenon is known as peripheral nerve stimulation (PNS) [21, 25, 44]. It can range in intensity from a harmless tingling sensation synced with the pulsing of the gradients, to serious pain and discomfort for the patient. PNS could be especially dangerous when occurring in or near cardiac tissue [18], though limits on  $dB/dt$  for PNS that are now too restrictive for this to be of concern to patients. The intensity to which PNS is experienced varies from patient to patient.

When the electric field is produced in the vicinity of an electrically conductive medical implant, the resultant voltage produces eddy currents in the device. These voltages can occur anywhere in the device, whether within a single electrical lead, between leads, or between electrodes and a conductive AIMD enclosure. However, in the context of eddy current safety, only planar surfaces are of concern for eddy currents. This may include the device enclosure, some internal circuitry, or battery components.

When the electric energy of the eddy current flows through the conductive material, it is converted into thermal power via resistive losses. At higher temperatures, device heating can damage the surrounding tissue [12, 14, 35].

For example, in the case of an idealized conductive disk used in test standards, the power deposited by eddy currents is proportional to the square of the  $dB/dt$  according to equation 1.3.1.

$$P = \sigma T \pi \frac{R^4}{8} \left( \frac{dB}{dt} \cos \beta \right)^2 \quad (1.3.1)$$

Here,  $\sigma$  is the conductivity of the material,  $T$  is the device thickness,  $R$  is the device radius, and  $\beta$  is the angle of the  $dB/dt$  with respect to the normal vector of the disc, reflecting the importance of device orientation within the scanner. In general, maximum heating occurs when the  $dB/dt$  is orthogonal to the surface of the device. Since  $dB/dt$  depends on a square term, even small changes can result in significant differences in heating. The effect of heating increase with distance from the magnetic isocentre [37]. Gradient coils are designed such that they produce a linear field gradient over the imaging region, adding or subtracting from the main field depending on the direction from the isocenter. Thus, the farther a point is from the isocenter, the greater the change in field as the current changes polarity.

Gradient induced vibrations are also possible. Unlike the typical vibrations that may occur on a device as a result of a patient's day to day activity, for gradient induced vibrations, the forces are not external to the device. Vibrations are also most common on conductive planar surfaces. When an eddy current is induced on a surface, it produces a time dependent magnetic moment that will interact with the static main magnetic field. This torque produces vibrations of the device, which can be very dangerous for patients [25].

The higher the  $dB/dt$  values are, the greater their effect on devices and patients. However, as mentioned above, for the sake of image quality and imaging time, it is also desirable for gradients to be stronger and faster. Thus, it is important not to be too conservative with  $dB/dt$  limitations while still maintaining patient safety during scanning procedures.

## 1.4 Classification of medical devices

The American Food and Drug Administration (FDA) recommends all medical device testing be performed in accordance to procedures outlined in the safety standards published by the American Society for Testing and Materials (ASTM). These regulatory documents outline standard testing methods and safety limits. The standard relevant to this research is outlined in ISO/TS 10974 [25]. Across the whole range of devices that may be found in the MR environment, when all the possible interactions described above have been investigated, a device can be given one of three classifications:

- **MR Safe** – The device poses no known hazards within the MR environment. MR Safe items are made of materials that are non-conductive, non-metallic, and non-ferromagnetic.
- **MR Conditional** – The device has demonstrated safety in the MR environment within certain specific conditions. Scanning is allowed only when these limits are upheld. Determining just what these specific conditions are poses a significant challenge. Conditions can include limits on device positioning, field strength, etc.
- **MR Unsafe** – No conditions exist under which the device has been shown to be safe, and as such it poses unacceptable risks within the MR environment [26, 23].

## 1.5 Research objectives

In this investigation, we seek to develop a simulation tool to predict the fields produced by MRI gradient coils. Current safety standards described in ISO/TS 10974 [25] for  $dB/dt$  exposure only discuss the maximum  $dB/dt$  that a device may be exposed to when within the scanner. While this is important information for determining the safety of devices in the context of gradient coils, the average over the device is also very relevant for device safety. From Faraday's law, any voltages induced in a conductive surface or volume depend on the flux of the field across the entire volume of the device. In order to better inform regulatory labeling, this thesis seeks to quantify the effect that spatial averaging will have on  $dB/dt$  exposure values for realistic device volumes within the MRI environment.

## Chapter 2: Validation of Biot-Savart $dB/dt$ modelling software

### 2.1 Introduction

The main objective of this thesis is to systematically investigate the magnetic fields produced across a range of different scanner and device configurations that medical implants may face, as well as to investigate the effects of spatial averaging on  $dB/dt$  exposure in order to ensure that device safety limitations are not too conservative in the context of MRI gradients while still guaranteeing patient safety. The first task was to develop a software system that can be used for that investigation, and then to validate the software by comparing its predictions to physical measurements.

To perform this validation, a physical magnetic coil system was constructed for which a detailed software model of the coil wire patterns existed. Measurements were taken of the field produced by this coil under standard operation by a field probe.

Then, a simulation was conducted using the known coil wire pattern, and the probe used to take the measurements was modelled. The simulated results were found to agree with experimental results within a mean difference of 5.1%.

## 2.2 Methods

### 2.2.1 Experimental setup

A resistive coil was constructed intended for use as a  $dB/dt$  device safety testing platform, based on the designed high-resolution numerical model. This coil consisted of 2 layers of axial wire pairs with an inner radius of 22.40 cm. The constructed coil is shown in the midground of figure 2.2-1. It had an efficiency of 0.0937 mT/A. The constructed coil was connected to a PCI2100 amplifier. This amplifier was used to produce a 25 T/s rms sine waveform at 270 Hz, a common test configuration outlined in ISO/TS 10974 [25], producing a  $dB/dt$  field within the volume of the coil.

The field produced by this coil was measured using the induction probe shown in figure 2.2-1. The probe operated according to Faraday's law of induction, whereby the  $dB/dt$  produced by the coil induced a voltage in loops of wire. The leads of the wire loops of the probe were connected to an 8-bit oscilloscope, allowing measurements of the voltages induced in the loops. To relate the voltages to the  $dB/dt$ , a conversion factor for the probe of 51 (T/s)/V was used, derived from the area of the 5.0 cm diameter loops and the 10 wire windings per axis. The probe had 3 perpendicular axes in total, allowing measurements of all the vector components of the field. Only the data from the loop that was oriented along the z axis of the coil (the axis oriented along the bore of the coil) was considered for comparison with numerical values.

Using a robotic positioning system, the probe was positioned throughout the volume of the bore of the coil to take measurements of the field. The robotic system is shown in the foreground of figure 2.2-2. It consists of an extended arm holding the probe, controlled by a set of three Nema 23 stepper motors and driven with a software controller, allowing the precise positioning of the probe at arbitrary points in three-dimensional space. The volume over which the probe was positioned consisted of  $x$ - and  $y$ -positions from -15 cm to 15 cm and  $z$ -positions from -15 cm to 10 cm, as constrained by the cylindrical bore of the coil, with the point ( $x = 0$  cm,  $y = 0$  cm,  $z = 0$  cm) being the isocenter of the magnet, and a step size of 1 cm in each direction.

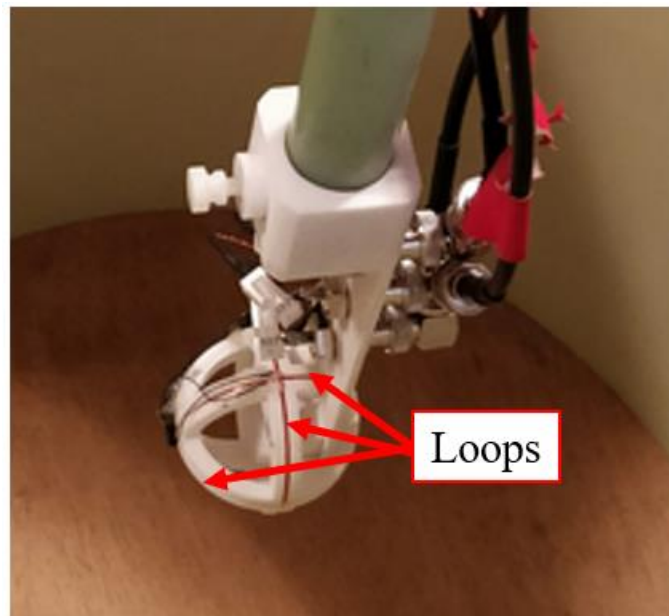


**Figure 2.2-1:** The probe used to collect  $dB/dt$  measurements. The probe had 3 axes corresponding to the Cartesian axes, with the three loops consisting of 10 loops of copper wire each with a 5.0 cm loop diameter, shown by the arrows. The set of loops hidden by the lip of the white mound corresponds to the  $z$  axis in this case, since it has its normal oriented along the bore of the coil.





**Figure 2.2-2:** The experimental setup. In the foreground is the robotic system used to collect the field data over the volume of the  $dB/dt$  coil, the cylindrical system in the midground. The grey regions contain the wire windings of the coil.

### 2.2.2 Simulation

The same wire pattern used in the prefabrication design of the  $dB/dt$  coil was used for the simulations. It is shown in figure 2.2-3. It consisted of a two-layer split solenoid, had an inner radius of 22.40 cm and a split distance of 7.69 cm. The wire pattern is discretized into 3008 sections of infinitesimal diameter, with each section having an  $xyz$ -coordinate for its center,  $dx$ ,  $dy$ , and  $dz$  elements representing the length of the section and a value for the electrical current in amperes running through that section of the coil. For this design, all sections of the coil had the same

current. The contribution of each wire component is added together in a Biot-Savart law calculation. For more details on how the  $dB/dt$  is related to the magnetic field, refer to the appendix, where details on field calculations are discussed for readers of both chapters 2 and 3.

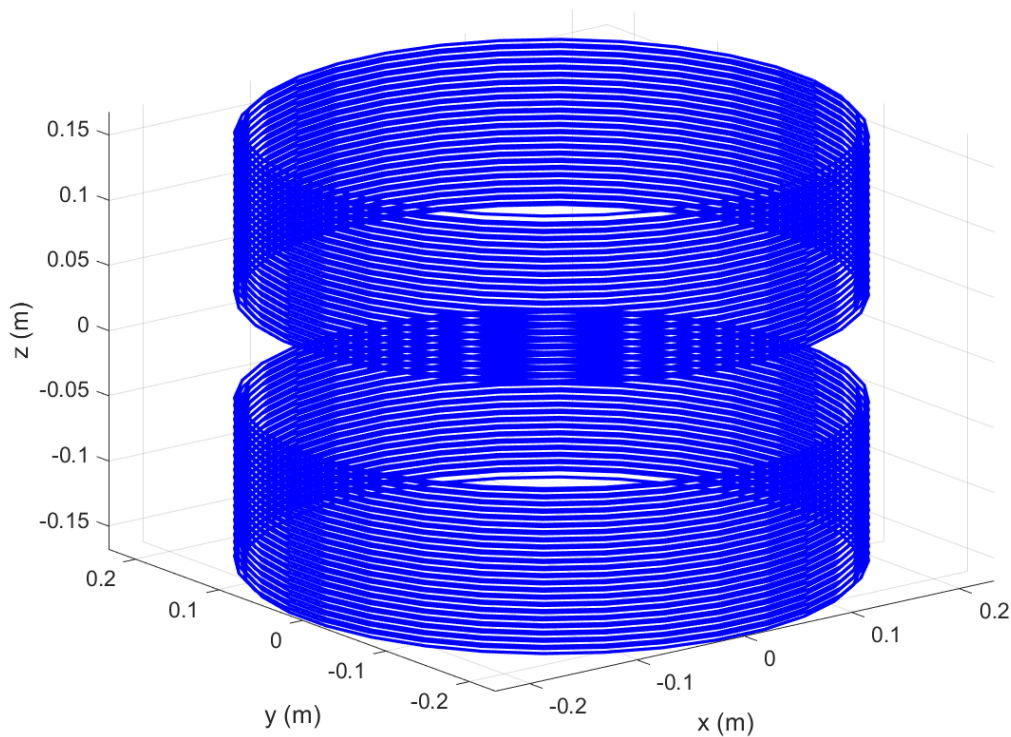


**Figure 2.2-3:** The wire pattern on the  $dB/dt$  coil. The coil is a large bore split solenoid. Visible are the two radially stacked layers of wire windings, with the inner layer having 24 windings, and the outer layer having 23.

The  $z$  loop of the probe, meaning the loop whose normal was oriented along the bore of the coil, shown in figure 2.2-2 was modelled as a circle with a 5.0 cm diameter at a 0.5 mm resolution, resulting in 7860 points over the surface of the interior of the loop. This simulated device area is shown in figure 2.2-4. The device area was positioned at the same locations that measurements were taken within the

bore of the coil, with  $x$ - and  $y$ - positions varying from -15 cm to +15 cm away from the isocenter of the coil, as constrained by the geometry of the coil, and  $z$ -positions varying from -15 cm to +10 cm from isocenter. For each position within the coil, the field over the loop area is calculated at each of the 7860 points into which it is discretized, and the average value is taken. This value is then compared to the measurement from the probe at that position.

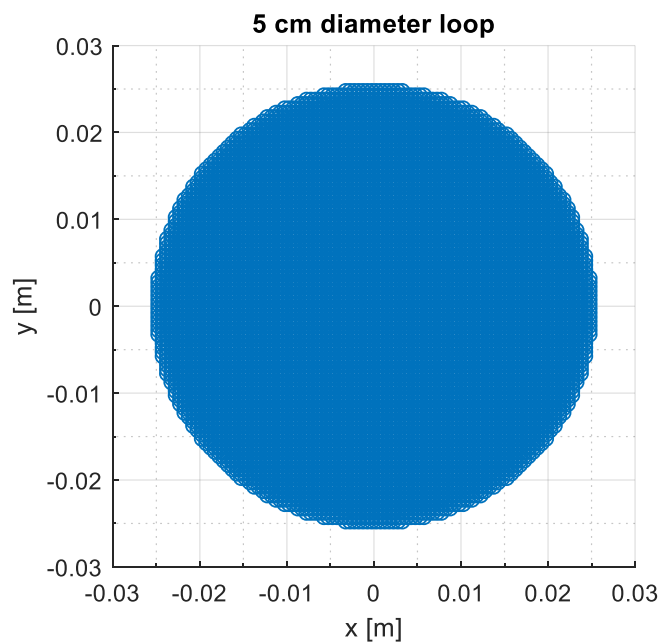


**Figure 2.2-4:** The simulated loop of the probe, being the region over which spatial averaging was performed. This area had a 5.0 cm diameter and a surface discretization of 0.5 mm, resulting in 7860 points on the device. The  $dB/dt$  is calculated at each one of these points, and an average is taken.

## 2.3 Results

Across all the positions at which measurements were taken, the measured values differed from predictions by an average of 4.9%. The median error was 4.8%, and the maximum error over the volume of interest was 11.7%. Shown below in figures 2.3-1 and 2.3-2 are the simulated and measured fields for a sample region along the  $xz$ -plane. Figure 2.3-3 shows the percent difference between the results in figures 2.3-1 and 2.3-2. Figure 2.3-4 also shows a distribution of percent differences, but for the plane  $z = -10$  cm. Figure 2.3-5 shows the distribution of differences between simulated results and measurements across the whole measurement volume. Figure 2.3-6 shows the distribution of the fields for the simulated and measured cases. Finally, figure 2.3-7 compares the simulated and measured values compared against the ideal case.

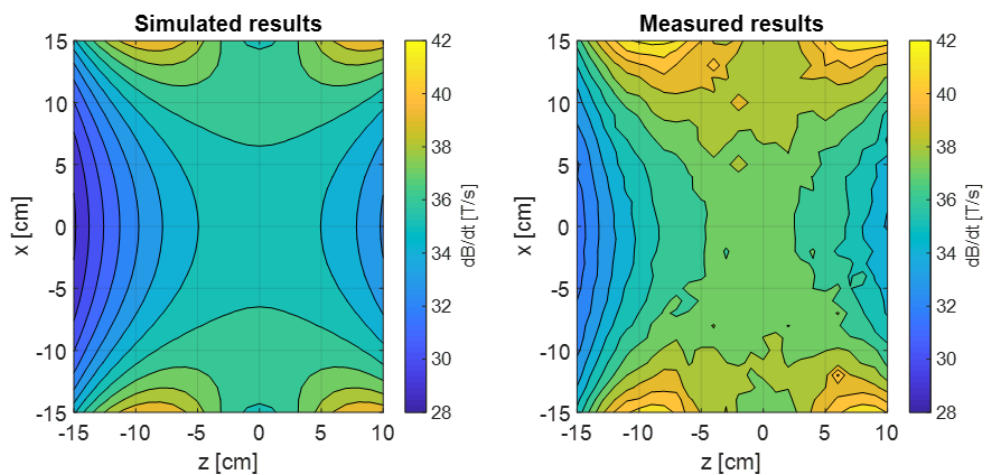


**Figure 2.3-1 (left):** The spatial distribution of the simulated  $dB/dt$  within the bore for the plane  $y = 0$  cm. Note that the  $z$ -direction is along the bore of the coil.

**Figure 2.3-2 (right):** The spatial distribution of the measured  $dB/dt$  within the bore of coil for the plane  $y = 0$  cm. Note that the  $z$ -direction is along the bore of the coil.

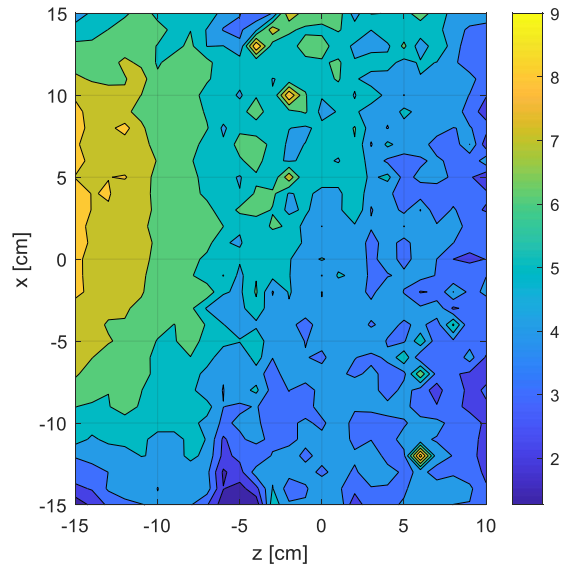


**Figure 2.3-3:** The spatial distribution of percent differences between the measured and simulated values within the bore of coil for the plane  $y = 0$  cm. Note that the  $z$ -direction is along the bore of the coil. The asymmetry in the extent in the  $z$ -direction the measurements is a result of the limitations of the reach of the positioning system.

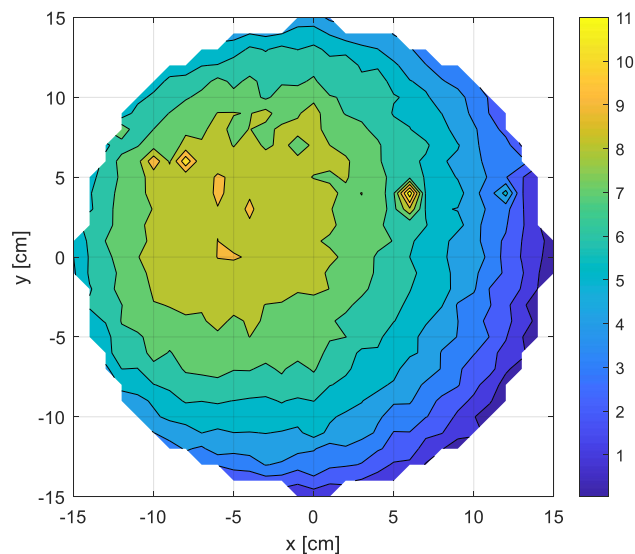


**Figure 2.3-4:** The spatial distribution of percent differences between the measured and simulated values within the bore of coil for the plane  $z = -10$  cm. Note that the  $z$ -direction is along the bore of the coil.

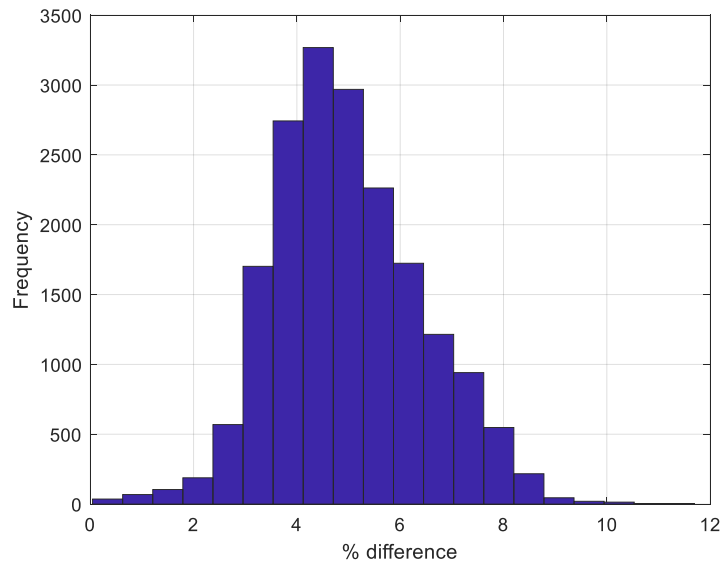


**Figure 2.3-5:** A histogram of the percent differences between the measured values and the simulated data. The distribution of the errors is influenced by the precision limitations of the oscilloscope used to major the induced voltages, which in turn determine the measured  $dB/dt$  values.

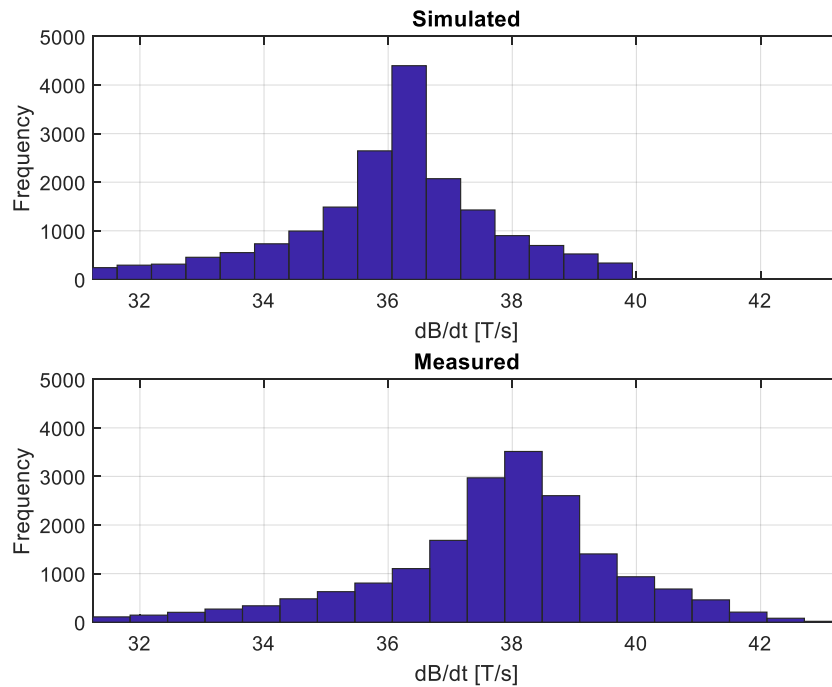


**Figure 2.3-6:** Histograms of the  $dB/dt$  distributions for both the simulated (top) and measured (bottom) values. Note the systematic difference between the two. The simulation consistently underpredicts the measurements.

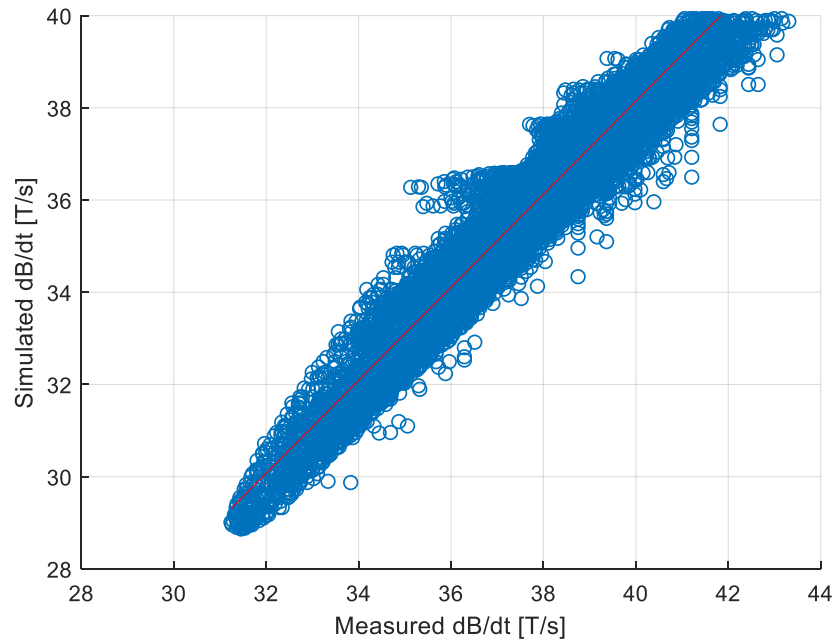


**Figure 2.3-7:** A comparison between the predicted field values along  $y$ , and the measured values along  $x$ . The ideal case of perfect equality is shown overlaid in red.

## 2.4 Discussion

From figures 2.3-6 and 2.3-7, it is evident that there is some systematic error in the simulated results when compared to the measurements. The measured values are consistently higher than simulated values. The error is also asymmetrically distributed in space. Figure 2.3-3 shows that the greatest error between the predictions and the measurements occurs in the negative  $z$  region.

This error is the result of several factors. The manufacturing tolerances used in the construction of the coil resulted in small differences between the physical coil and the design model. Exact quantification of these differences is not possible with the coil windings now being set inside opaque epoxy. An offset

in the wire radius and separation would result in this systematic error. To best measurement, the measured radius was found to be less than it was designed to be. Considering this change an offset was found to account for up to a 2% shift in the simulated results. Additionally, an offset in the split between the two halves of the coil along the bore direction produces a difference between the model and the constructed coil, leading to the observed increased error in the negative  $z$  region. Additionally, a miscalibration of the function generator used to provide the  $dB/dt$  waveforms and the probe results in a systematic error in the results.

Note that as described above, the voltages from the probe were collected using an oscilloscope. This oscilloscope was limited to 8-bits when taking measurements, reducing the precision of the values. This influences the spread of the errors shown in figure 2.3-5.

Based on the comparison between the simulated results and the actual measurements, with the mean difference across the whole measurement space being less than 5%, it was concluded that the simulation can predict results within reasonable uncertainty, and that this tool could be used to start investigating the effect of averaging over more arbitrary devices inside actual gradient coil designs.



## Chapter 3: The effect of spatial averaging on $dB/dt$ exposure values

### 3.1 Introduction

The objective of this investigation was to determine the effect that spatial averaging would have on predicted  $dB/dt$  values within realistic MRI gradient systems. The safety testing standard ISO/TS 10974:2018(E) [25] contains simulated data describing the peak  $dB/dt$  values that active implantable medical devices (AIMDs) could be exposed to when within varying volumes within the bore of MRI scanners.

For devices with realistic spatial extent, to understand the  $dB/dt$  relevant for testing, information about the spatial average  $dB/dt$  value over the device needs to be known as well as the peak  $dB/dt$ . Clearly the average  $dB/dt$  value will be smaller than the peak values described in 10974, but the question remains as to how much are they decreased. Here, these differences between the peaks and spatial averages over the volume of a 5.0 cm diameter sphere are investigated.

## 3.2 Methodology

To quantify the effects of spatial averaging, a volume was defined over which this averaging was performed. The interactions of this example device volume, a 5.0 cm diameter sphere, were investigated over the range of MRI gradient coils described in Annex A of ISO/TS 10974:2018(E) [25]. This volume of space for averaging was chosen because of its similar spatial extent to certain AIMDs relevant for testing with 10974. In practice, to understand the interactions of a specific device, spatial averaging would have to be quantified for that device's unique geometry.

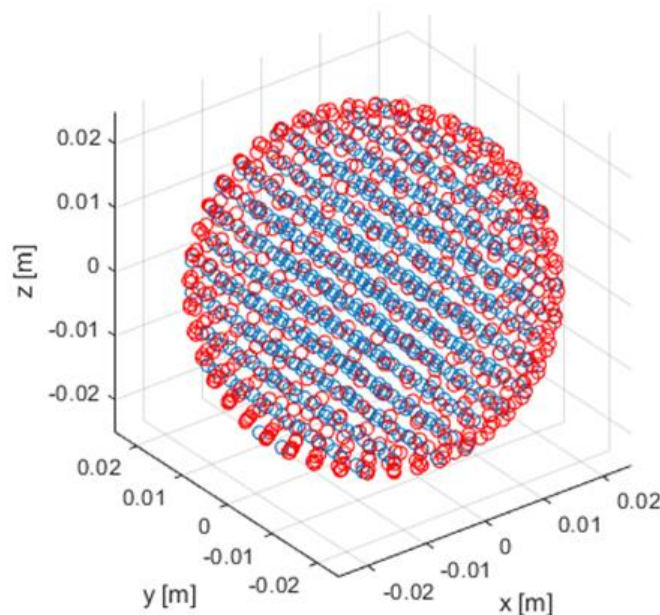


**Figure 3.2-1:** The 5.0 cm diameter spherical volume used as the ‘device’ in these simulations, with the points on the surface in red and the points in interior in blue. The blue points are discretized in a grid with a 5 mm separation between points along each axis. The red points are equal in number to the blue points but equally spaced over the spherical surface.

The device volume was simulated as a 5.0 cm diameter sphere (figure 3.2-1). The interior of the device was discretized in a 5 mm rectangular Cartesian grid, with a total of 552 points. The surface of the device was subdivided more finely, with the same number of equally spaced points as there were points on the interior of the device. The surface was subdivided using by using a gradient descent algorithm designed to minimize the electrostatic potential energy of a system of charged particles equal to the desired number of points. The surface was more finely subdivided in this way to get more information about the locations that are closest to the coils of the gradient, where highest  $dB/dt$  exposure will occur. The magnetic field was calculated over the device volume using Biot-Savart methods in MATLAB and the average and peak fields were determined for each location, within each coil.

The range of gradient coils were designed for previous editions of 10974 to represent most possible gradient coil designs that would be found in clinical MRI systems. The ability to survey many different scanner types in a relatively short amount of time is an obvious advantage of simulation over physical testing. With all the different combinations included, a total of 224 different gradient coils were considered.

Three-axis coil ( $G_x$ ,  $G_y$ ,  $G_z$ ) sets which corresponded to both 60 cm and 70 cm inner diameter MRI systems were modeled using previously developed and validated methods [19]. These gradient coils were designed with lengths of 140, 150, 160, and 170 cm. For each length the size of the imaging region varied over:

35, 40, 45, and 50 cm. The imaging region is a volume, usually spherical, where the magnet is most homogeneous and the gradients are most linear.

For each of the designs, the field produced by all seven axis combinations of the three gradient axes was separately evaluated, namely the  $G_x$ ,  $G_y$  and  $G_z$  on their own, as well as  $G_{xy}$ ,  $G_{xz}$ ,  $G_{yz}$  and  $G_{xyz}$ . This was to ensure that any possible scenario that could arise during an imaging sequence was investigated.

For each of these gradient coil designs, the magnetic field was calculated to find the  $dB/dt$ . As described in the appendix, for the frequencies at which gradient coils operate, the  $dB/dt$  is proportional to the magnetic field by some constant factor. To determine the field for each of these seven different gradient axis combinations, it was necessary to determine the correct efficiency for each. Using the arrays of discretized elements for each gradient coil as determined using the methods described in [19], the efficiency was calculated for the individual  $x$ ,  $y$  and  $z$  gradients. These efficiencies were then added in quadrature depending on the combination being simulated.

For each gradient coil design considered, the local  $dB/dt$  levels produced were calculated over a device volume positioned at each point over the surface of a compliance volume within the gradient coil. Depending on the position within the gradient coil, the device would naturally be subjected to different magnetic field environments. For MR conditional status, which enforces specific limits on the conditions under which a patient can be imaged, the effect is considered at various distances from the center of the coils. The closer the device is located to the wire windings of the coils, the greater the field it will be exposed to due to inverse-square

nature of the Biot-Savart law, but patients are usually located closer to the central axis of the coil. A device that wouldn't ever be positioned close to the windings would not be held to that  $dB/dt$  exposure standard.

To simulate the fields within each of the gradient designs considered, it was necessary to determine where within those gradients the device volume should be positioned. A range of different positioning grid parameters (tables 3.2-1 and 3.2-2) were investigated for the compliance volume, namely the step size along the axis of the bore ( $z$  step) and the angular resolution. They were considered for a single coil case, for the 60 cm inner diameter, 160 cm length, 45 cm imaging region coils, at a 25 cm compliance radius, which was around the middle of the set of coils used. Each combination of the three gradient axes was considered for this coil test.

$z$ step [cm]	Spatially averaged $dB/dt$ [T/s]				Peak $dB/dt$ [T/s]			
	$dB_x/dt$	$dB_y/dt$	$dB_z/dt$	$dB/dt$	$dB_x/dt$	$dB_y/dt$	$dB_z/dt$	$dB/dt$
<b>1</b>	89.6	86.4	78.3	90.1	102	97.9	90.8	104
<b>5</b>	88.8	85.7	76.7	90.1	102	97.6	89.2	104
<b>10</b>	88.8	85.7	76.4	90.1	102	97.6	88.8	104

**Table 3.2-1:** The spatially averaged  $dB/dt$  compared to the peaks at three different step sizes in  $z$  for the 60 cm inner diameter, 160 cm length, 45 cm imaging region coils, at a 25 cm compliance radius. The angular resolution was at 10 degrees. A  $z$  step of 10 cm was decided upon for the simulations of the final family of coils as a trade off to still have a reasonable runtime.

Angular step [degrees]	Spatially averaged $dB/dt$ [T/s]				Peak $dB/dt$ [T/s]			
	$dB_x/dt$	$dB_y/dt$	$dB_z/dt$	$dB/dt$	$dB_x/dt$	$dB_y/dt$	$dB_z/dt$	$dB/dt$
<b>1</b>	88.8	85.7	76.4	90.1	102	97.6	88.7	104
<b>5</b>	88.8	85.7	76.4	90.1	102	97.6	88.7	104
<b>10</b>	88.8	85.7	76.4	90.1	102	97.6	88.7	104

**Table 3.2-2:** The spatially averaged  $dB/dt$  compared to the peaks at three different step sizes in the angular spacing for the 60 cm inner diameter, 160 cm length, 45 cm imaging region coils, at a 25 cm compliance radius. A  $z$  step of 10 cm was used. An angular step of 10 degrees was decided upon for the simulations of the final family of coils as a trade off to still have a reasonable runtime.

In the  $z$  step test in table 3.2-1, when the step size is increased to 5 cm, the maximum error is only 2.1%. When the step size is increased to 10 cm, the maximum error is only 2.5%. For the angular step test in table 3.2-2, once the  $z$  step had been set in the previous test, there was no appreciable difference in the results when increasing the step size from 1 degree to 10 degrees. The purpose of this investigation was to quantify the impact of spatial averaging, with less focus on what the peaks are, which had already been investigated in the preparation of a previous edition of 10974. When considering the differences between the spatially averaged values and the peaks for the  $z$  step test in table 3.2-1, the differences between the two are shown in figure 3.2-3. The largest difference was only 0.9%. In the angular case, there was again no appreciable difference across the different step sizes.

<i>z</i> step [cm]	Percent difference			
	$dB_x/dt$	$dB_y/dt$	$dB_z/dt$	$dB/dt$
<b>1</b>	12.9	12.5	14.8	14.3
<b>5</b>	13.8	13.0	15.1	14.3
<b>10</b>	13.8	13.0	15.0	14.3

**Table 3.2-3:** The percent difference between the spatially averaged  $dB/dt$  (left side of table 3.2-1) and the peaks (right side of table 3.2-1) by component and magnitude of the  $dB/dt$  vector. Three different step sizes in  $z$  are shown for the 60 cm inner diameter, 160 cm length, 45 cm imaging region coils, at a 25 cm compliance radius.

From the results in these tables, it was decided that the grid on which the device volume would be positioned within each gradient coil would be composed of 777 points, with 21 groups of points from -1 m to 1 m positioned 10 cm apart in the  $z$ -direction (along the bore of the gradients) by 37 angular groups of points 10 degrees apart (figure 3.2-2). These values were chosen to decrease the run time while still preserving enough detail. Even with the coarser parameters chosen, the simulations can take over a week in order to survey the entire parameter space.

With the discretization of the positioning grid decided, several radii of that grid were simulated. The radius of the cylindrical positioning grid was such that when the device was placed at some point on its surface, the edge of the device would be located at some ‘compliance radius’. Five different compliance radii were simulated for each gradient axis combination: 10, 15, 20, 25, and 30 cm. For the 20 cm case, for example, since the device volume was 5.0 cm in diameter, the radius of the set of points would be 17.5 cm (as shown in figure 3.2-2) so that the edge of the device volume was at the 20 cm compliance radius. In all cases (other than table

3.3-1), the  $dB/dt$  values are normalized against the applied gradient slew rate. To convert the values into  $dB/dt$ , they need to be multiplied by the desired single-axis gradient slew rate. In table 3.3-1, a gradient slew rate of 200 T/m/s is used.

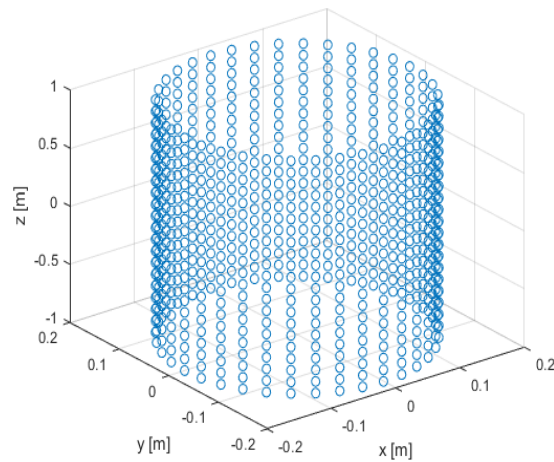


**Figure 3.2-2:** The calculation grid for the 20 cm compliance radius case. Note that the radius is slightly less than 20 cm at 17.5 cm so that the 5.0 cm diameter device volume with its center at any point on this grid will extend to 20 cm at most.

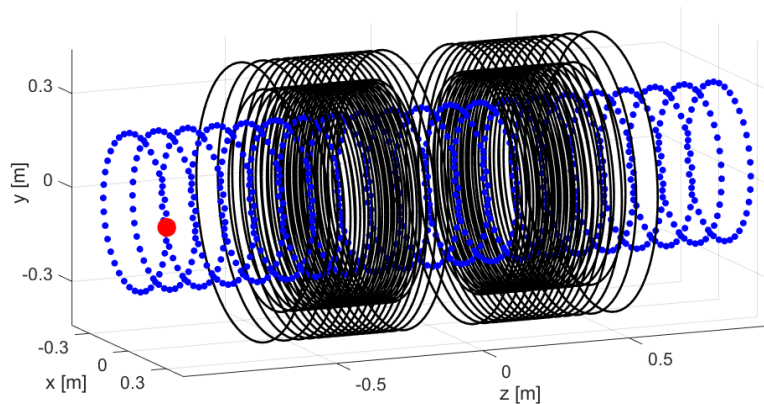


**Figure 3.2-3:** The 5.0 cm diameter spherical device in red at a single point of the surface of one compliance radius. The compliance radius it located within a single example gradient, the 60 cm inner diameter, 140 cm length, and 35 cm imaging region, for the  $z$  gradient, shown in black. The blue points, extending from -1 m to 1 m, represent each position at which the device is positioned and simulated for each coil combination.



### 3.3 Results

The results obtained across the five different compliance radii are shown in table 3.3-1. The  $dB/dt$  is broken down into its cartesian components, the average magnitude of the  $dB/dt$ , as well as the peak  $dB/dt$  for each cartesian component and the magnitude. Figure 3.3-1 shows the distribution across the 777 points for a single example coil. Figure 3.3-2 shows the distribution for the entire family of coils simulated. Figure 3.3-3 shows the peak spatially averaged values across the family of coils broken down by compliance radius and the gradient axis combination.

Compliance Radius [m]	Spatially averaged $dB/dt$ [T/s]				Peak $dB/dt$ [T/s]			
	$dB_x/dt$	$dB_y/dt$	$dB_z/dt$	$dB/dt$	$dB_x/dt$	$dB_y/dt$	$dB_z/dt$	$dB/dt$
0.10	59.4	59.2	60.8	63.0	61.6	61.4	62.2	65.2
0.15	64.6	64.2	64.2	68.0	68.6	68.0	66.8	72.0
0.20	73.6	72.8	69.8	77.2	80.6	79.2	74.6	83.6
0.25	89.0	87.2	82.8	91.6	101	98.0	92.4	102
0.30	114	110	104	116	132	126	117	135

**Table 3.3-1:** The maximum  $dB/dt$  by compliance radius for the family of coils at a slew rate of 200 T/m/s. Note that the  $dB/dt$  component labels shown above do not correspond to gradient axes but indicate the components of the  $dB/dt$  vector. The right-most three columns list the peak (no spatial averaging) values obtained for the individual  $dB/dt$  components. Note also that the magnitude column does not correspond to the quadrature sum of the peak  $x$ -,  $y$ -,  $z$ -components of the  $dB/dt$ , but rather is the peak of all the magnitudes in the calculation region.

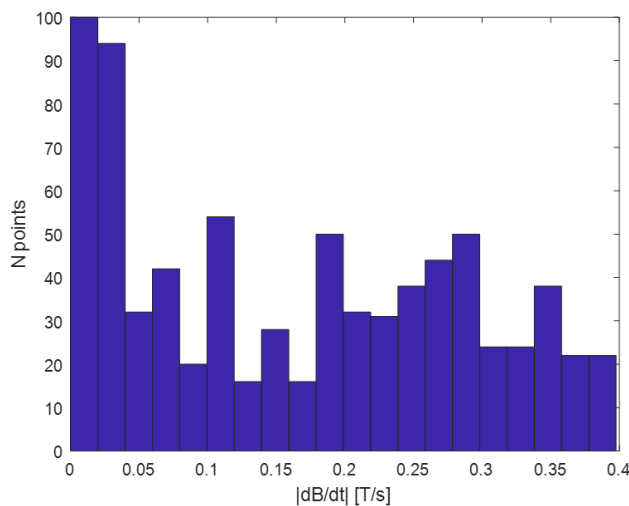


**Figure 3.3-1:** Histogram of the  $dB/dt$  (magnitude) at all 777 points within one example coil:  $x$  gradient of 60 cm diameter, 160 cm length, 45 cm imaging region coil at a 25 cm compliance radius. Values are given as  $dB/dt$  per unit slew rate of the gradient axes. For a 200 T/m/s scanner system, the values above need to be multiplied by 200.

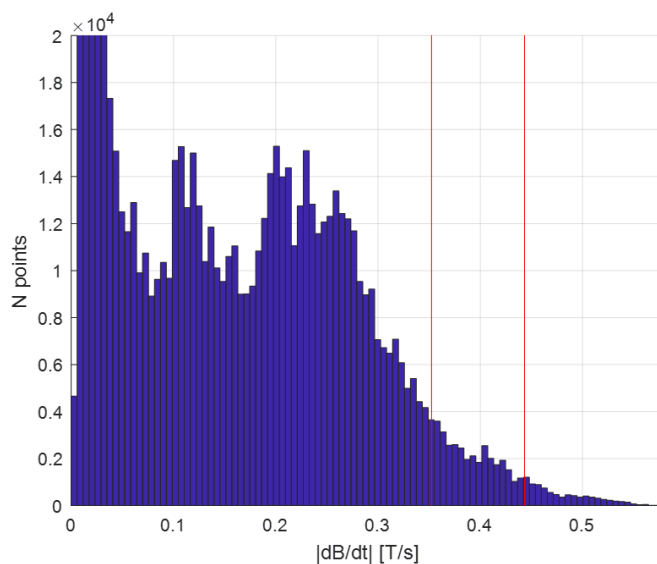


**Figure 3.3-2:** Histogram of all the data across all the coils (and all compliance volumes) with the 95th and 99th percentiles shown (0.352 T/s per slew rate and 0.443 T/s per slew rate). For a 200 T/m/s scanner system, the values above need to be multiplied by 200.

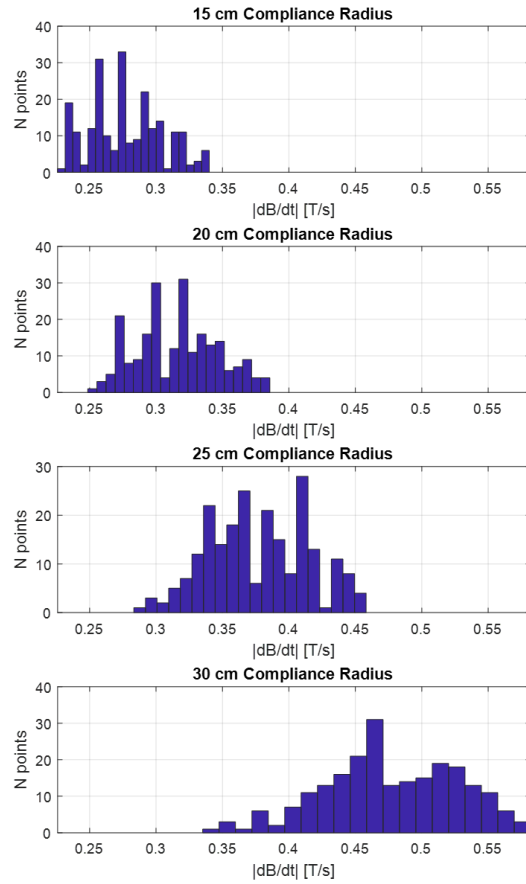


**Figure 3.3-3:** The peak spatially averaged  $dB/dt$  value across each coil in the simulation space at 4 different compliance radii. Values are given as  $dB/dt$  per unit slew rate of the gradient axes. For a 200 T/m/s scanner system, the values above need to be multiplied by 200.

### 3.4 Discussion

From the information in table 3.3-1, and the distributions in figure 3.2-3, it is evident that the maximum  $dB/dt$  the device experiences increases with compliance radius. A higher  $dB/dt$  is experienced closer to the windings of the gradients, as expected from the inverse-square nature of the Biot-Savart law. For a 5.0 cm diameter spherical device, across a range of compliance radii from 10 cm to 30 cm radius the highest spatially-averaged  $dB/dt$  value that could possibly be experienced across all the combinations of device location and gradient coil design at a slew rate of 200 T/m/s is 116 T/s. From the histograms in figures 3.3-1 and 3.3-2, the  $dB/dt$  values a device experiences are dominated by the smaller values, both in the single gradient case in figure 3.3-1, and across the family of coils, shown in figure 3.3-2. Clearly there will be some decrease when considering the spatial averages compared to the peaks.

From table 3.3-1, the mean and peak values differ between 2 and 17%. The difference between the peak and mean values increases monotonically, as expected, with compliance radius. Devices positioned closer to the gradient coils themselves would see this reduction most strongly. The location of maximum  $dB/dt$  exposure on a specific device must of course be considered when evaluating safety, with knowledge of those locations on the device where this exposure would be the most dangerous. Because the power deposited in a conducting surface depends on the square of the  $dB/dt$ , even small changes in the  $dB/dt$  to which a device is exposed during testing can have a large impact on the observed physical effects.

With this new information in mind, if spatially averaged information were included in 10974 in the future, it would allow for better understanding of what a medical device experiences and allow for more appropriate limitations on  $dB/dt$ , and more devices could pass tests while still ensuring that patients are safe. Because of the general nature of the simulations developed in this research, the effect of spatial averaging could also be investigated over a range of different device geometries, on a case-by-case basis, when evaluating specific device safety.

## Appendix A: Simulating $dB/dt$ values

### A.1 Simulating $dB/dt$

To calculate the  $dB/dt$  at any location in space and time around the gradient coil, the magnetic field per unit current (T/A) at the location of interest is multiplied by the time-derivative of the current (A/s), which can be related to the so-called slew rate of the coil. The time rate of change of magnetic gradient fields ( $G(t)$ ) during operation is defined by this slew rate ( $SR$ ), measured in T/m/s (A-1). There is only one slew rate value for a gradient coil at any given time, so the same slew rate value is used for every location at which the  $dB/dt$  is calculated. [25]

$$SR(t) = \frac{dG(t)}{dt} \quad (\text{A-1})$$

Although the magnetic fields and the magnetic field gradients produced by a gradient coil are spatially varying, only a single value of gradient strength is defined for a gradient coil: the gradient strength per unit current (the gradient efficiency,  $\eta$ , in T/m/A) at the geometric center (isocenter) of the MR system.

For the purposes of this investigation, to find the  $dB/dt$ , a relationship between the  $dB/dt$  and the gradient slew rate at any location within the gradient coil is required. Since the gradient strength is proportional to the instantaneous current [44] through the coil by the gradient efficiency:

$$G(t) = \eta I(t) \quad (\text{A-2})$$

Equations A-1 and A-2 can be combined, and when solving for the time-derivative of the current:

$$\frac{d I(t)}{dt} = \frac{1}{\eta} SR(t) \quad (\text{A-3})$$

The magnetic field at any location in space and time can also be expressed in such a way that it is proportional to the instantaneous current through the coil:

$$\vec{B}(\vec{r}, t) = \vec{b}(\vec{r}) I(t) \quad (\text{A-4})$$

Here,  $\vec{b}(\vec{r})$  is the local vector magnetic field per unit current (T/A) at any location. In the simulations performed in this thesis, all calculations of this local vector magnetic field are determined using the Biot-Savart law (A-5).

$$\vec{B}(\vec{r}) = \frac{\mu_0}{4\pi} \int_C \frac{I \vec{dl} \times \hat{r}'}{|\vec{r}'|^2} \quad (\text{A-5})$$

Here,  $\vec{B}$  is the magnetic flux density described in tesla,  $\mu_0$  is the vacuum permeability in henries per meter,  $I$  is the current in amperes,  $\vec{dl}$  is an infinitesimal length of the wire conductor in meters, and  $\vec{r}'$  is the vector representing the distance between the conductor element and the point at which the  $\vec{B}$  field is calculated. For the purposes of the spatial averaging simulations, a unit current is used, so the field determined by the Biot-Savart law calculations is equivalent to the local vector magnetic field per unit current (T/A). As noted in the introductory chapter, because of the relatively low-frequency operation of gradient coils, the system can be well approximated as quasi-static. This means that no wavelength or retarded potentials need to be considered in the field calculations. Time variation is completely

separable from spatial variation, and fields within the volume can be simulated as if no biological tissues were present using these Biot-Savart calculations.

Continuing with the relationship defined above in equation A-4, taking the time derivative yields:

$$\frac{d}{dt} \vec{B}(\vec{r}, t) = \vec{b}(\vec{r}) \frac{dI(t)}{dt} \quad (\text{A-6})$$

Combining A-3 and A-6, the relationship between instantaneous gradient slew rate and the instantaneous  $dB/dt$  at any location  $\vec{r}$  in space can be expressed as:

$$\frac{d}{dt} \vec{B}(\vec{r}, t) = \left( \frac{\vec{b}(\vec{r})}{\eta} \right) SR(t) \quad (\text{A-7})$$

The factor in brackets in equation A-7 is the ratio of the vector magnetic field at any location  $\vec{r}$  in space, divided by the gradient efficiency value (A-2). This factor has units of meters but does not correspond to an actual location within the gradient coil, and so it should be combined with the slew rate to be meaningful. It is a vector quantity, independent of time. In the results presented in chapter 3, the results are often presented either as this  $dB/dt$  factor, or the slew rate scaled  $dB/dt$  itself. The captions of any figures showing results note whether any conversion needs to take place.



## A.2 Simulating spatial averages

To calculate the spatially averaged  $dB/dt$  over any volume within the bore of an arbitrary gradient coil operating at some slew rate, a discrete average is taken over the equation A-7, as shown in equation A-8. In the context of this research, the volume over which the discrete average is performed is meant to be representative of the volume that a typical medical implant might occupy, and so it is referred to in this thesis as a ‘device volume’.

$$\frac{1}{N} \sum_{i=1}^N \frac{d}{dt} \vec{B}_i(t) = \frac{1}{N} \sum_{i=1}^N \left( \frac{\vec{b}_i(\vec{r})}{\eta} \right) SR(t) \quad (\text{A-8})$$

Here,  $N$  is the number of points that are averaged over, and  $\eta$  is the gradient efficiency, as before. Note that depending on the geometry of the device volume, the orientation of the  $dB/dt$  relative to that volume is very important in understanding the effects of the  $dB/dt$  on a physical device, so all of the vector components of the  $dB/dt$  need to be considered. The device volume is discretized into  $N$  voxels of equal size. Simplifying gives:

$$\frac{d}{dt} \vec{B}_{average}(t) = SR(t) \cdot \frac{1}{N} \sum_{i=1}^N \left( \frac{\vec{b}_i(\vec{r})}{\eta} \right) \quad (\text{A-9})$$

### A.3 Combining gradient fields

Previously, only the simulated fields produced by a single gradient coil were considered. However, MRI gradient coils contain an  $x$ -,  $y$ - and  $z$ -gradient, any combination of which may be used in an MRI pulse sequence. When calculating the spatially averaged  $dB/dt$  for a coil combination, each of their magnetic fields and slew rates must be incorporated. Consider equation A-9 from above, now with three different contributions:

$$\frac{d}{dt} \bar{B}_{average}(t) = \frac{1}{N} \sum_{i=1}^N \left( \frac{\vec{b}_i^{G_x}(\vec{r})}{\eta_{G_x}} \right) SR_{G_x} \left( \frac{\vec{b}_i^{G_y}(\vec{r})}{\eta_{G_y}} \right) SR_{G_y} \left( \frac{\vec{b}_i^{G_z}(\vec{r})}{\eta_{G_z}} \right) SR_{G_z} \quad (\text{A-10})$$

Where  $\vec{b}_i^{Gradient}(\vec{r})$  is the magnetic field per unit current at location  $i$  produced by one of the gradients, either  $x$ ,  $y$  or  $z$ , and there are  $N$  elements of equal size over which the average is performed, with the three gradient axes operating at their own individual slew rates and with their own gradient efficiencies.

The case of combined gradient axis operation considered in this thesis is when all three are driven at the same slew rate, 200 T/m/s. In order to convert the  $dB/dt$  factors into the proper  $dB/dt$  values, the slew rate of the individual axes must be used. If each axis is driven at a slew rate of 200 T/m/s, then the slew rate for the  $dB/dt$  calculation must also be 200 T/m/s, not an effective three-axis combined slew rate of 346 T/m/s. In this case, the equation becomes:

$$\frac{d}{dt} \bar{B}_{average}(t) = SR_{200} \frac{1}{N} \sum_{i=1}^N \left( \frac{\vec{b}_i^{G_x}(\vec{r})}{\eta_{G_x}} \frac{\vec{b}_i^{G_y}(\vec{r})}{\eta_{G_y}} \frac{\vec{b}_i^{G_z}(\vec{r})}{\eta_{G_z}} \right) \quad (\text{A-11})$$

It is assumed that there is the same time-dependence in both the spatially averaged  $dB/dt$  and the slew rate. To compute the combined  $dB/dt$  factor in brackets in the summation, the field values  $\vec{b}_i$  found by the Biot-Savart law at each location and each axis combination are scaled by the efficiency, then summed and averaged. These factors are obtained over the entire device volume for each location within the gradient coil set.

For these simulations, any combination of the three simultaneous gradient axes are considered numerically as a single effective coil with an effective gradient efficiency (the quadrature sum of the constituent axis efficiencies) operating at the gradient slew rate of interest.

The field calculation for this combined coil involves the Biot-Savart law summation over the wire patterns of all three axes together, and the average  $dB/dt$  value would become:

$$\frac{d}{dt} \vec{B}_{average}(t) = SR_{200} \frac{1}{N} \sum_{i=1}^N \left( \frac{\vec{b}_i^{eff}(\vec{r})}{\eta_{eff}} \right) \quad (\text{A-12})$$

When considering the  $dB/dt$  factors in an analysis of their distribution, histograms of these factors were produced, and the peaks and spatial averages were compared to quantify the effect of spatial averaging. All simulations were performed in MATLAB [2].

## References

- [1] E. M. Haacke, R. W. Brown, M. R. Thompson, and R. Venkatesan. (1999). *Magnetic Resonance Imaging: Physical Principles and Sequence Design*, vol. 1st.
- [2] The Mathworks Inc., “MATLAB - MathWorks”, [www.mathworks.com/products/matlab](http://www.mathworks.com/products/matlab), 2017. [Online]. Available: <http://www.mathworks.com/products/matlab/>
- [3] McRobbie, D. W., Moore, E. A., Graves, M. J., & Prince, M. R. (2006). *MRI From Picture to Proton* (2nd ed.). New York: Cambridge University Press
- [4] “10 Facts About MRIs”. Medical Associates of Northwest Arkansas. <https://www.mana.md/10-facts-about-mris/>
- [5] “Ionizing Radiation, Health Effects and Protective Measures.” World Health Organization, World Health Organization, [www.who.int/news-room/fact-sheets/detail/ionizing-radiation-health-effects-and-protective-measures](http://www.who.int/news-room/fact-sheets/detail/ionizing-radiation-health-effects-and-protective-measures).
- [6] Canadian Institute for Health Information (CIHI). (2012). “Medical Imaging in Canada”.
- [7] Canadian Agency for Drugs and Technologies in Health (CADTH). (2018). “The Canadian Medical Imaging Inventory, 2017”.
- [8] Kalin, R., & Stanton, M. S. (2005). Current clinical issues for MRI scanning of pacemaker and defibrillator patients. *PACE - Pacing and Clinical Electrophysiology*, 28(4), 326–328
- [9] F. G. Shellock and A. Spinazzi. (2008). “MRI Safety Update 2008: Part 2, Screening Patients for MRI”, *Am. J. Roentgenol.*, vol. 191, no. 4, p. 1140–1149.
- [10] A. M. Sawyer-Glover and F. G. Shellock. (2000). “Pre-MRI procedure screening: Recommendations and safety considerations for biomedical implants and devices”, *Journal of Magnetic Resonance Imaging*, vol. 12, no. 1, p. 92–106.

- [11] C. S. Simpson and A. M. Gillis. (2006). “The pacemaker and implantable cardioverter defibrillator recall issue - a Canadian perspective.”, *Canadian Journal of Cardiology*, vol. 22, no. 6, p. 467–71
- [12] Nyenhuis, J. A., Park, S.-M., Kamondetdacha, R., Amjad, A., Shellock, F. G., & Rezai, A. R. (2005). MRI and Implanted Medical Devices: Basic Interactions with an Emphasis on Heating. *IEEE Transactions on Device and Materials Reliability*, 5(3), 467–480
- [13] J. Starčuková, Z. Starčuk, H. Hubálková, and I. Linetskiy. (2008) “Magnetic susceptibility and electrical conductivity of metallic dental materials and their impact on MR imaging artifacts”, *Dental Materials*, vol. 24, no. 6, p. 715–723.
- [14] J. S. Shinbane, P. M. Colletti, and F. G. Shellock. (2011). “Magnetic resonance imaging in patients with cardiac pacemakers: era of ‘MR Conditional’ designs.”, *Journal of Cardiovascular Magnetic Resonance*, vol. 13, no. 1, p. 63.
- [15] F. G. Shellock and V. J. Shellock. (1996). “Vascular access ports and catheters: Ex vivo testing of ferromagnetism, heating, and artifacts associated with MR imaging”, *Magnetic Resonance Imaging*, vol. 14, no. 4, p. 443–447.
- [16] Courtesy of Allen D. Elster, MRIquestions.com
- [17] “MRI EGC sagittal”. Wikimedia Commons.  
[upload.wikimedia.org/wikipedia/commons/5/5f/MRI\\_EGC\\_sagittal.png](https://upload.wikimedia.org/wikipedia/commons/5/5f/MRI_EGC_sagittal.png)
- [18] Davids, Mathias & Guerin, Bastien & Malzacher, Matthias & Schad, Lothar & Wald, Lawrence. (2017). Predicting Magnetostimulation Thresholds in the Peripheral Nervous System using Realistic Body Models. *Scientific Reports*. 7. 10.1038/s41598-017-05493-9.
- [19] C.T. Harris, D.W. Haw, W.B. Handler, B.A. Chronik. (2013) “Shielded resistive electromagnets of arbitrary surface geometry using the boundary element method and a minimum energy constraint”. *Journal of Magnetic Resonance*. 234:95-100.

- [20] ISO ISO 13485:2016. Medical devices - Quality management systems - Requirements for regulatory purposes
- [21] Ham, C. L., Engels, J. M., van de Wiel, G. T. and Machielsen, A. (1997). Peripheral nerve stimulation during MRI: Effects of high gradient amplitudes and switching rates. *Journal of Magnetic Resonance Imaging*, 7: 933-937.
- [22] Maisel, W. H. (2004). Medical Device Regulation: An Introduction for the Practicing Physician. *Annals of Internal Medicine*, 140, 294–302
- [23] Woods, T. O. (2007). Standards for Medical Devices in MRI: Present and Future. *Journal of Magnetic Resonance Imaging*, 26, 1186–1189.
- [24] ISO 13485. International Organization for Standardization (ISO). (2016). “Medical devices — Quality management systems — Requirements for regulatory purposes”
- [25] ISO/TS 10974. International Organization for Standardization (ISO). (2018). Assessment of the safety of magnetic resonance imaging for patients with an active implantable medical device.
- [26] ASTM F2503/13. “Standard Practice for Marking Medical Devices and Other Items for Safety in the Magnetic Resonance Environment”,
- [27] Projectile Cylinder Accidents Resulting from the Presence of Ferromagnetic Nitrous Oxide or Oxygen Tanks in the MR Suite  
Gregory Chaljub, Larry A. Kramer, Raleigh F. Johnson, III, Raleigh F. Johnson, Jr., Harbans Singh, and Wayne N. Crow  
*American Journal of Roentgenology* 2001 177:1, 27-30
- [28] F. G. Shellock, T. O. Woods, and J. V. Crues. (2009). “MR Labeling Information for Implants and Devices: Explanation of Terminology”, *Radiology*, vol. 253, no. 1, p. 26–30.
- [29] T. Birkholz, M. Schmid, C. Nimsky, J. Schüttler, and B. Schmitz. (2004). “ECG artifacts during intraoperative high-field MRI scanning.”, *Journal of Neurosurgical. Anesthesiology*, vol. 16, no. 4, p. 271–6.

- [30] D. Formica et al. (2004). “Biological effects of exposure to magnetic resonance imaging: an overview”, *Biomedical Engineering Online*, vol. 3, no. 1, p. 11.
- [31] OECD. (2014). *Magnetic resonance imaging (MRI) exams, total. Health: Key Tables.*
- [32] J. F. Schenck. (2000). “Safety of Strong, Static Magnetic Fields”, *Journal of Magnetic Resonance Imaging*, vol. 12, no. 1, p. 2–19.
- [33] C. Landrigan. (2001). “Preventable Deaths and Injuries during Magnetic Resonance Imaging”, *New England Journal of Medicine*, vol. 345, no. 13, p. 1000–1001.
- [34] R. P. Klucznik, D. A. Carrier, R. Pyka, and R. W. Haid. (1993) “Placement of a ferromagnetic intracerebral aneurysm clip in a magnetic field with a fatal outcome.”, *Radiology*, vol. 187, no. 3, p. 855–856.
- [35] T. R. Oskar Talcoth and T. Rylander. (2011) “Electromagnetic Modeling of Pacemaker Lead Heating During MRI”.
- [36] Collins CM, Wang Z. (2011). Calculation of radiofrequency electromagnetic fields and their effects in MRI of human subjects. *Magnetic Resonance in Medicine* 65:1470.
- [37] Graf, H., Steidle, G., & Schick, F. (2007). Heating of metallic implants and instruments induced by gradient switching in a 1.5-Tesla whole-body unit. *Journal of Magnetic Resonance Imaging*, 26(5), 1328–1333.
- [38] ASTM International. (2015). *Standard Test Method for Measurement of Magnetically Induced Displacement Force on Medical Devices in the Magnetic Resonance Environment.*
- [39] ASTM International (2017). *Standard Test Method for Measurement of Magnetically Induced Torque on Medical Devices in the Magnetic Resonance Environment.* 2017.
- [40] ASTM International. (2011). *Standard Test method for Measurement of Radio Frequency Induced Heating on or Near Passive Implants During Magnetic Resonance Imaging.*

- [41] F. G. Shellock and J. V. Crues, “High-field-strength MR imaging and metallic biomedical implants: An ex vivo evaluation of deflection forces”, *Am. J. Roentgenol.*, vol. 151, no. 2, p. 389–392, 1988.
- [42] J. Planert, H. Modler, and R. Vosshenrich, “Measurements of magnetism-related forces and torque moments affecting medical instruments, implants, and foreign objects during magnetic resonance imaging at all degrees of freedom”, *Medical Physics*, vol. 23, no. 6, p. 851– 856, 1996.
- [43] Kanal E, Shellock FG, Talagala L. (1990). Safety considerations in MR imaging. *Radiology* 176:593–606.
- [44] Chronik, B. A. and Rutt, B. K. (2001), Simple linear formulation for magnetostimulation specific to MRI gradient coils. *Magn. Reson. Med.*, 45: 916-919. doi:10.1002/mrm.1121



# Curriculum Vitae

**Name:** Christopher Andrew Philip Brown

**Post-secondary** Western University

**education and degrees:** London, Ontario, Canada

2012-2017

B.Sc.

Major in Physics

Major in Computer science

Honors

Western University

London, Ontario, Canada

2017-present

M.Sc.

Physics

**Honors and Awards:** WUSRA

NSERC

Dean's Honour List

Physics and Astronomy TA Award

**Related Work** Summer Research Student

**Experience:** Western University

2013-2017

**Conferences Proceedings:** “The effect of spatial averaging on  $dB/dt$  exposure values for implanted medical devices”

Abstract Submission

International Society of Magnetic Resonance in  
Medicine, (2019)

Montreal, QC

“The effect of spatial averaging on  $dB/dt$  exposure values for implanted medical devices”

Abstract Submission

Imaging Network of Ontario, (2019)

London, ON